Developmental Biology 459 (2020) 109–125

Contents lists available at ScienceDirect

Developmental Biology

journal homepage: www.elsevier.com/locate/developmentalbiology

CFAP43 modulates ciliary beating in mouse and *Xenopus*

Ev Rachev [a], Karin Schuster-Gossler [a], Franziska Fuhl [b], Tim Ott [b], Lena Tveriakhina [a], Anja Beckers [a], Jan Hegermann [c], Karsten Boldt [d], Michaela Mai [a,2], Elisabeth Kremmer [e,1], Marius Ueffing [d], Martin Blum [b,*], Achim Gossler [a,**]

[a] Institute for Molecular Biology, OE5250, Hannover Medical School, Carl-Neuberg-Str. 1, 30625, Hannover, Germany
[b] Institute of Zoology, University of Hohenheim, Garbenstraße 30, 70593, Stuttgart, Germany
[c] Institute of Functional and Applied Anatomy, Research Core Unit Electron Microscopy, Hannover Medical School, Carl-Neuberg-Str. 1, 30625, Hannover, Germany
[d] Institute of Ophthalmic Research, Center for Ophthalmology, University of Tübingen, Röntgenweg 11, 72076, Tübingen, Germany
[e] Institute of Molecular Immunology, Helmholtz Zentrum München, German Research Center for Environmental Health (GmbH), Core Facility Monoclonal Antibodies, Marchioninistr. 25, 81377, München, Germany

ARTICLE INFO

Keywords:
CFAP43
Ciliogenesis
Cilia
Hydrocephalus
Mucociliary clearance
Male infertility
Xenopus laevis
Mouse

ABSTRACT

Malfunctions of motile cilia cause a variety of developmental defects and diseases in humans and animal model organisms. Defects include impaired mucociliary clearance of the airways, sperm immotility, hydrocephalus and organ laterality. Here, we characterize the evolutionary conserved *Cfap43* gene by loss-of-function experiments in the mouse and the frog *Xenopus laevis*. *Cfap43* is expressed in tissues carrying motile cilia and acts as a target gene of the transcription factor FOXJ1, which is essential for the induction of motile ciliogenesis. We show that CFAP43, a protein of unknown biochemical function, localizes to the ciliary axoneme. CFAP43 is involved in the regulation of the beating frequency of tracheal cilia and loss of CFAP43 causes severe mucus accumulation in the nasal cavity. Likewise, morphant and crispant frog embryos revealed impaired function of motile cilia of the larval epidermis, a model for airway mucociliary epithelia. CFAP43 participates in the formation of flagellar axonemes during spermatogenesis as mice mutant for *Cfap43* display male infertility, consistent with observations in male sterile patients. In addition, mice mutant for *Cfap43* display early onset hydrocephalus. Together, these results confirm the role of CFAP43 in the male reproductive tract and pinpoint additional functions in airway epithelia mucus clearance and brain development.

1. Introduction

Cilia project from the surface of many eukaryotic cells into the extracellular space and are pivotal for normal development and tissue homeostasis (Gerdes et al., 2009; Praveen et al., 2015). Their core, the axoneme, is composed of nine peripheral microtubule doublets, with or without attached motor proteins, and possesses two central microtubules or not. Cilia are classified as motile or not, and cells bearing motile cilia may be mono- or multiciliated (reviewed in Takeda and Narita, 2012). Cells with motile cilia either propel themselves, such as for example the sperm cell, or move fluids along the cell surface. During early mammalian and amphibian development, motile monocilia at the left-right organizer (LRO) generate a leftward fluid flow that is essential for the establishment of the asymmetric arrangement of visceral organs (Blum and Ott, 2018a; Yoshiba and Hamada, 2014). The coordinated beating of hundreds of motile cilia on epithelial cells of the respiratory tract in mice or the epidermis of *Xenopus* larvae (multiciliated cells, MCCs) is essential for mucociliary clearance (Jain et al., 2010; Stannard and O'Callaghan, 2006). MCCs lining the brain ventricles generate flow of the cerebrospinal fluid (CF), which is required for brain development and function (Banizs et al., 2005; Jacquet et al., 2009; Lee, 2013; Spassky et al., 2005). In fallopian tubes, MCCs move egg cells into the ampulla and preimplantation embryos towards the uterus (Lyons et al., 2006). Motile cilia in the pronephric ducts of frog embryos propel urine from the pronephros to the cloaca, contributing to urine excretion and water homeostasis (reviewed in Getwan and Lienkamp, 2017).

* Corresponding author.
** Corresponding author.
E-mail addresses: martin.blum@uni-hohenheim.de (M. Blum), gossler.achim@mh-hannover.de (A. Gossler).
[1] present address: Department of Biology II, Ludwig-Maximilians University, Groβhaderner Straβe 2, 82,152 Martinsried, Germany.
[2] present address: DMSG Bundesverband, Krausenstr. 50, 30,171 Hannover, Germany.

https://doi.org/10.1016/j.ydbio.2019.12.010
Received 16 September 2019; Received in revised form 14 December 2019; Accepted 18 December 2019
Available online 27 December 2019

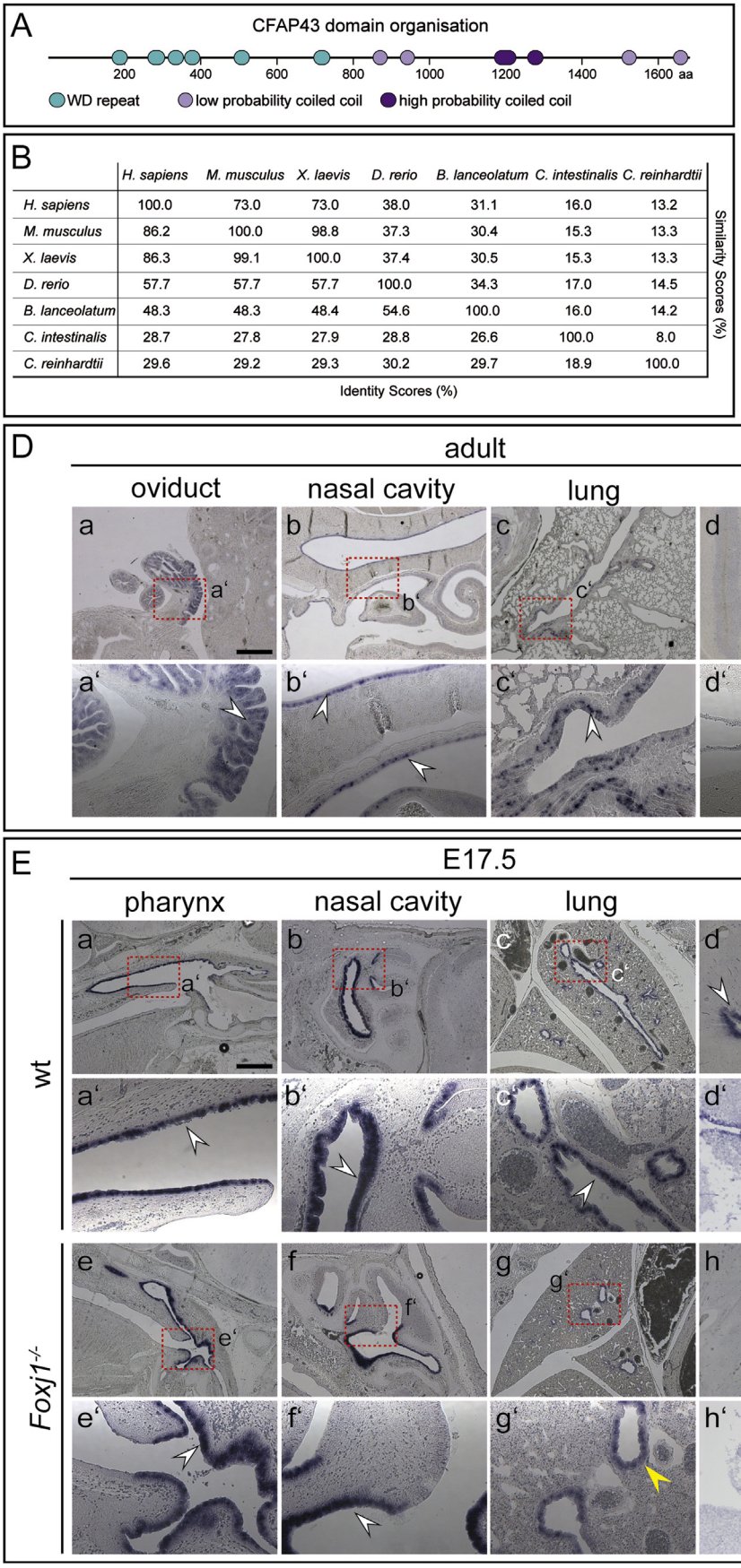

	H. sapiens	M. musculus	X. laevis	D. rerio	B. lanceolatum	C. intestinalis	C. reinhardtii
H. sapiens	100.0	73.0	73.0	38.0	31.1	16.0	13.2
M. musculus	86.2	100.0	98.8	37.3	30.4	15.3	13.3
X. laevis	86.3	99.1	100.0	37.4	30.5	15.3	13.3
D. rerio	57.7	57.7	57.7	100.0	34.3	17.0	14.5
B. lanceolatum	48.3	48.3	48.4	54.6	100.0	16.0	14.2
C. intestinalis	28.7	27.8	27.9	28.8	26.6	100.0	8.0
C. reinhardtii	29.6	29.2	29.3	30.2	29.7	18.9	100.0

Fig. 1. Murine *Cfap43* is expressed in tissues carrying multiciliated cells.
(A) Murine CFAP43 protein contains 6 WD-repeats in the N-terminal part (Uniprot, (https://www.uniprot.org/uniprot/E9Q7R9), whereas the C-terminus contains six coiled-coil domains, as predicted by Multicoil (http://cb.csail.mit.edu/cb/multicoil/cgi-bin/multicoil.cgi). **(B)** Similarity matrix of CFAP43 amino acid sequences from different species reveals high evolutionary conservation. **(C)** *Cfap43* is expressed in the left-right organizer (LRO, arrowhead) at E8.25 (lateral (a) and ventral view (b)) as detected by WISH. **(D)** *Cfap43* expression in wt adult mouse tissues was detected by SISH (a-d; red boxes are magnified in a'-d'). White arrowheads in (a'-d') point to regions of expression. **(E)** *Cfap43* expression in E17.5 wt (a-d; red boxes are magnified in a'-d') and *Foxj1*$^{-/-}$ (e-h; red boxes are magnified in e'-h') tissues was detected by SISH (marked by white arrowheads). Note that *Cfap43* expression was reduced in the lung epithelium (g, yellow arrowhead in g') and absent in the ependymal layer and choroid plexus (CP) of *Foxj1*$^{-/-}$ specimens (red arrowheads in h, h'). Scale bars: Da-d, Ea-h = 500 μm.

Impaired or disrupted cilia motility leads, depending on the affected cilia type and species, to reduced mucociliary clearance and respiratory malfunctions, abnormal asymmetric arrangement of the inner organs, male and female infertility as well as hydrocephalus (Lee, 2013; reviewed in Praveen et al., 2015). We identified *Cfap43* in microarray screens for genes that were up-regulated during the differentiation of ciliated cells in the fetal mouse lung and down-regulated in *Foxj1* mutants (Stauber et al., 2017). Patients heterozygous for a truncated CFAP43 protein were reported to develop normal pressure hydrocephalus (Morimoto et al., 2019), and homozygous missense and nonsense mutations in *CFAP43* were identified in sterile male patients with 'multiple morphological abnormalities of the sperm flagella' (MMAF (Coutton et al., 2018; Sha et al., 2017; Tang et al., 2017)). Other symptoms related to non-functional motile cilia were not reported from such patients. In mice, nonsense mutations of *Cfap43* resulted in a comparable sperm phenotype, again without reported additional defects in tissues carrying motile cilia (Coutton et al., 2018; Sha et al., 2017; Tang et al., 2017). Here we show that *Cfap43* expression correlates with the presence of motile cilia in mouse and frog embryos, as well as in adult mouse tissues. Endogenous CFAP43 protein localizes to the ciliary axoneme. Furthermore, we demonstrate that CFAP43 loss-of-function affects not only mouse sperm, but also brain ventricle development and ciliary beat frequencies in multiciliated cells of both the mouse airways and *Xenopus* embryonic skin: knockout mice as well as morphant and crispant frog embryos reveal defects in mucociliary clearance.

2. Results

2.1. Expression and localization of Cfap43 mRNA and protein in mouse and frog

Cfap43 encodes an evolutionary conserved protein of 1682 amino acids, which contains 6 predicted WD repeats in its N-terminal and 6 low/high probability coiled coil domains in its C-terminal region (UniProt Consortium, 2019; Wolf et al., 1997) (Fig. 1A, B). During embryonic mouse development, *Cfap43* mRNA was detected in the left-right organizer (LRO) at E8.25 (LRO; Fig. 1C). High expression levels of *Cfap43* correlated with the presence of motile cilia in adult tissues (Fig. 1D, and Fig. S1) and in E17.5 embryos (Fig. 1Ea-d, a'-d'). *Cfap43* transcripts were detected in epithelial cells lining the respiratory tract, in brain ependymal cells and the choroid plexus (Fig. 1D, Ea-d, a'-d'). In *Foxj1*-mutant E17.5 embryos (n=3), *Cfap43* mRNA was reduced in the large airways of the lung (yellow arrowhead in Fig. 1Eg'), and not detectable in ependymal cells and the choroid plexus (red arrowheads in Fig. 1Eh, h'). Surprisingly, no reduction was seen in MCCs of the nasal cavity and the upper respiratory tract (Fig. 1Ee, f, white arrows in e', f'). Similar to mouse, *cfap43* mRNA transcription correlated with *foxj1* expression and the presence of motile cilia in *Xenopus laevis* embryos (Fig. 2). Transcripts were detected in the LRO (gastrocoel roof plate, GRP), floor plate (FP), MCCs of the larval epidermis, nephrostomes, branchial chambers (BC), and stomach (stom.), but not clearly detectable in the brain (zona limitans intrathalamica, ZLI; subcommissural organ, SCO) (Fig. 2Ab-h''''). The dependence on *foxj1* was demonstrated in gain- and loss-of-function experiments: ectopic *cfap43* staining was seen on the injected side of stage 19 embryos unilaterally injected with *foxj1* mRNA (100% penetrance in 3 independent experiments with 15 injected embryos each; typical specimen shown in Fig. 2B). To investigate whether *foxj1* was strictly required for *cfap43* transcription, a sgRNA was designed to target the *foxj1* locus (Fig. S2). Crispant specimens revealed that *cfap43* transcripts were drastically reduced (Fig. 2C), with residual staining retained in the proctodeum (black arrowhead in Fig. 2Cb). Reductions were observed in every crispant analyzed (3 experiments; 15 specimens each). Of note, formation of externally visible hydrocephalus was not recorded in *foxj1* crispants up to stage 45, i.e. before tadpoles start feeding and metamorphosis commences.

To study expression and localization of CFAP43 protein, we generated

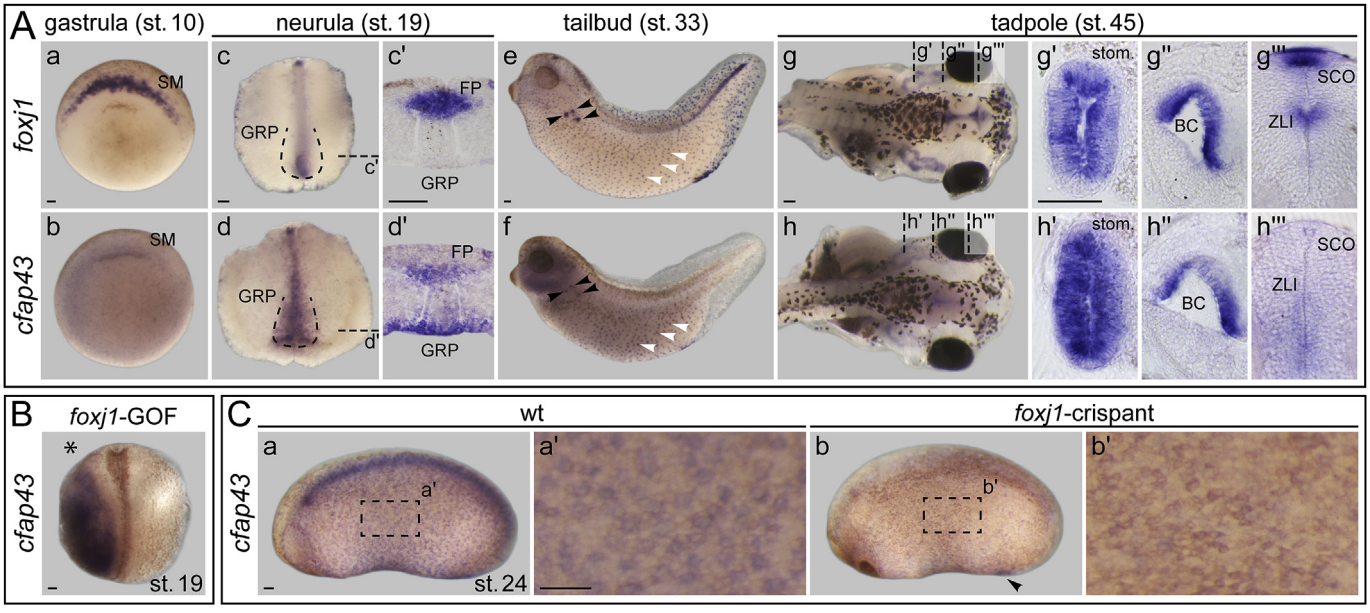

Fig. 2. Expression of *cfap43* in wt and *foxj1*-manipulated *Xenopus* embryos.
(A) *Foxj1* and *cfap43* are co-expressed as shown by comparative analysis of *foxj1* and *cfap43* mRNA expression in staged embryos using specific antisense RNA probes. (a, b) *foxj1* expression, but not *cfap43* was shown in the precursor of the left-right organizer (LRO), the superficial mesoderm (SM) of stage 10 gastrula embryos. (c, d) Dorsal explants and transversal histological sections (c', d') through neurula embryos at stage 19 revealed mRNA transcription of both genes in the floor plate (FP), and *cfap43* mRNA in addition in the LRO (GRP; outlined by dashed lines), where expression is induced already at stage 15 (not shown). (e, f) Co-expression in the nephrostomes (black arrowheads) and MCCs (white arrowheads) of stage 33 larvae. (g, h) Staining of stage 45 tadpoles in whole-mounts demonstrated strong neural expression of *foxj1* in the sub-commissural organ (SCO), zona limitans intrathalamica (ZLI) and the FP, which was absent for *cfap43* (g''', h'''). Non-neural expression was found in the dorsal lining of the branchial chamber (BC) (g'', h'') and in the stomach (stom.) (g', h'). **(B)** *Cfap43* is a *foxj1* target gene. Embryos were unilaterally injected with *foxj1* mRNA and analyzed for *cfap43* expression. *, injected side. **(C)** *Foxj1* F0 crispant embryos (b, b') lacked detectable *cfap43* expression except for the proctodeum (black arrowhead). Scale bars = 100 μm.

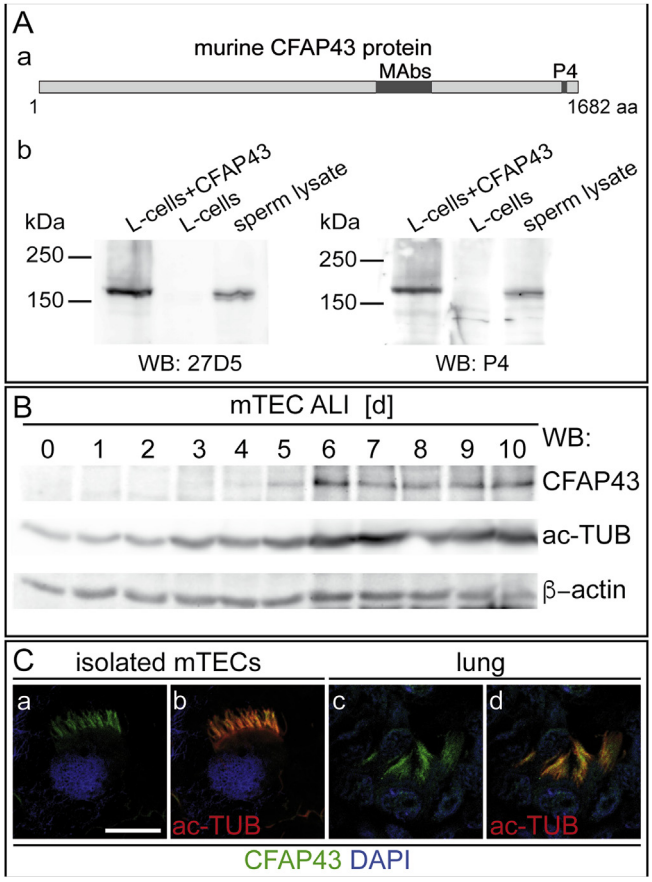

Fig. 3. Detection and subcellular localization of murine CFAP43.
(A) (a) A schematic representation of mouse CFAP43 protein showing regions used for immunization marked by dark gray boxes. (b) Western blot analyses of lysates from L-cells overexpressing CFAP43, untransfected L-cells, and wt mouse sperm lysates probed with monoclonal antibody 27D5 (left) or polyclonal antibody P4 (right). **(B)** Western blot analyses of mouse tracheal epithelial cells (mTECs) at various time points after initiation of air liquid interface (ALI) cultures probed for CFAP43 (27D5), acetylated α-tubulin (ac-TUB), and β-actin show upregulation of CFAP43 during ciliogenesis. **(C)** CFAP43 localizes to cilia in isolated mTECs (a, b) and lung sections (c, d), which were co-stained with monoclonal antibody 22A11 and acetylated α-tubulin (ac-TUB). Full size Western blots for Ab and B are shown in Figs. S9A and B. Scale bar in C = 10 μm.

specific antibodies directed against mouse CFAP43. Polyclonal rabbit antibodies were raised against a C-terminal peptide (P4, amino acids 1633–1647), while monoclonal rat and mouse antibodies (MAbs) were directed against a bacterially expressed polypeptide encompassing amino acids 1053–1226 (Fig. 3Aa). Western blot analyses detected CFAP43 in extracts from L-cells over-expressing the protein as well as endogenous protein in lysates of mouse sperm cells isolated from the cauda epididymis at the expected molecular weight of approximately 190 kDa (Fig. 3Ab). Endogenous CFAP43 was also detected in air-liquid interphase (ALI) cultures of mouse tracheal epithelial cells (mTECs), following the induction of ciliogenesis (Fig. 3B), consistent with the upregulation of *Cfap43* expression during fetal lung development (Stauber et al., 2017). In isolated mTECs (Fig. 3Ca, b) and in epithelial cells lining the lung airways (Fig. 3Cc, d), CFAP43 co-localized with acetylated-α-tubulin (ac-TUB), indicating localization of CFAP43 to motile cilia. This result is consistent with the localization of *Chlamydomonas* FAP43 to the inner dynein arm-associated tether and tether head complex (Fu et al., 2018; Kubo et al., 2018). In *Xenopus*, the polyclonal and monoclonal antibodies directed against mouse CFAP43 showed no specific signals (not shown). In summary, our expression analyses of *Cfap43* in mouse and frog demonstrate a tight correlation with motile cilia as well as a dependence on the transcription factor *Foxj1* at most of its expression sites.

2.2. Ciliary defects in Xenopus morphants and crispants

Cfap43 function was investigated in *Xenopus* embryos following gene knock-down using morpholino oligomers (MOs) and by genome editing using CRISPR/Cas9. Both translation and splice blocking MOs were used, referred to as TBMO and SBMO, respectively. MOs were injected at the 4-cell stage and targeted specifically to ciliated tissues and organs, namely the LRO, nephrostomes, skin, and brain. Targeting was controlled by co-injection of lineage tracer Alexa Fluor 488 dextran and pre-selection of correctly targeted specimens prior to phenotypic analysis. Both SBMO and TBMO resulted in a majority of embryos developing edema around the heart (tadpole cysts; Fig. S3A; raw data in Table S2), which can result from defective cardiac, lymphatic or nephrostome function (del Viso and Khokha, 2012). As *cfap43* was expressed in the developing nephrostomes (Fig. 2Af; raw data in Table S2), edema can be indicative of malfunctioning nephrostome cilia. The *Xenopus* tadpole skin harbors MCCs and mucus-producing cells and serves as a first line of defense against infections by MCC-driven mucus transport along the tadpole head-tail axis, functionally resembling MCCs of the mammalian airway epithelium (Blum and Ott, 2018b; Dubaissi and Papalopulu, 2011; Dubaissi et al., 2014; Walentek and Quigley, 2017). Hovering of tadpoles caused by ciliary beating of skin MCCs was reduced in tadpoles injected with TBMO, suggesting impaired ciliary function (Movie S1). Hydrocephalus and laterality defects were not observed in morphant specimens (Fig. S3B-E; raw data in Table S2).

Supplementary video related to this article can be found at https://doi.org/10.1016/j.ydbio.2019.12.010.

Because rescue experiments of morphant phenotypes, using HA-, GFP- or untagged mouse and *Xenopus* full-length constructs, failed, two guide RNAs (sgRNA1 and 2) were designed to edit the *cfap43* gene locus by CRISPR/Cas9 (Fig. S4). F0 specimens were analyzed for genome editing and ciliary phenotypes. LR defects, edemas and hydrocephalus were not observed (Fig. S3A, B, C). However, crispants displayed altered MCC motility (Movie S2). Remarkably, ciliary beat frequencies were markedly increased in morphant and crispant specimens, while cilia-driven transport of fluorescent beads along the anterior-posterior axis of stage 32 larvae was considerably reduced (Fig. 4A, B; Movies S2, S3; raw data in Table S1). IF staining of basal bodies and basal feet in skin MCCs revealed no differences between wildtype and crispant embryos (Fig. 4D). The lack of edemas in crispant specimens compared to morphants (Fig. S3A) could be the result of genetic compensation triggered by mutant mRNA degradation (El-Brolosy et al., 2019), which – however – has not been reported in *Xenopus* so far. In line with this formal possibility, *cfap43* transcripts were greatly reduced in crispant specimens (Fig. 4C). Genome editing thus confirmed a function of *cfap43* in the mucociliary epithelium of the tadpole skin, while additional motile cilia defects in morphant nephrostomes were either unspecific or compensated in crispants.

Supplementary video related to this article can be found at https://doi.org/10.1016/j.ydbio.2019.12.010.

2.3. Mucus accumulation, immobile sperm, and enlarged ventricles in Cfap43 knockout mice

To analyze the function of CFAP43 in mouse, we generated a conditional allele by flanking exon 3 (*ex3*) with loxP sites (Fig. 5A; Fig. S5). Deletion of exon 3 by Cre-mediated recombination results in a frame shift and termination of translation in exon 4 (*ex4*). Mutant mRNA, which might be degraded by nonsense-mediated decay, could still result in translation of an N-terminal polypeptide of 122 aa, encoded by exons 1 and 2 and followed by an additional 16 aa encoded by the shifted reading frame. To delete CFAP43 in all tissues we excised exon 3 in the female germ line ($Cfap43^{\Delta ex3}$) using ZP3:Cre mice (de Vries et al., 2000). Upon mating of heterozygous animals, homozygous $Cfap43^{\Delta ex3}$ mice were

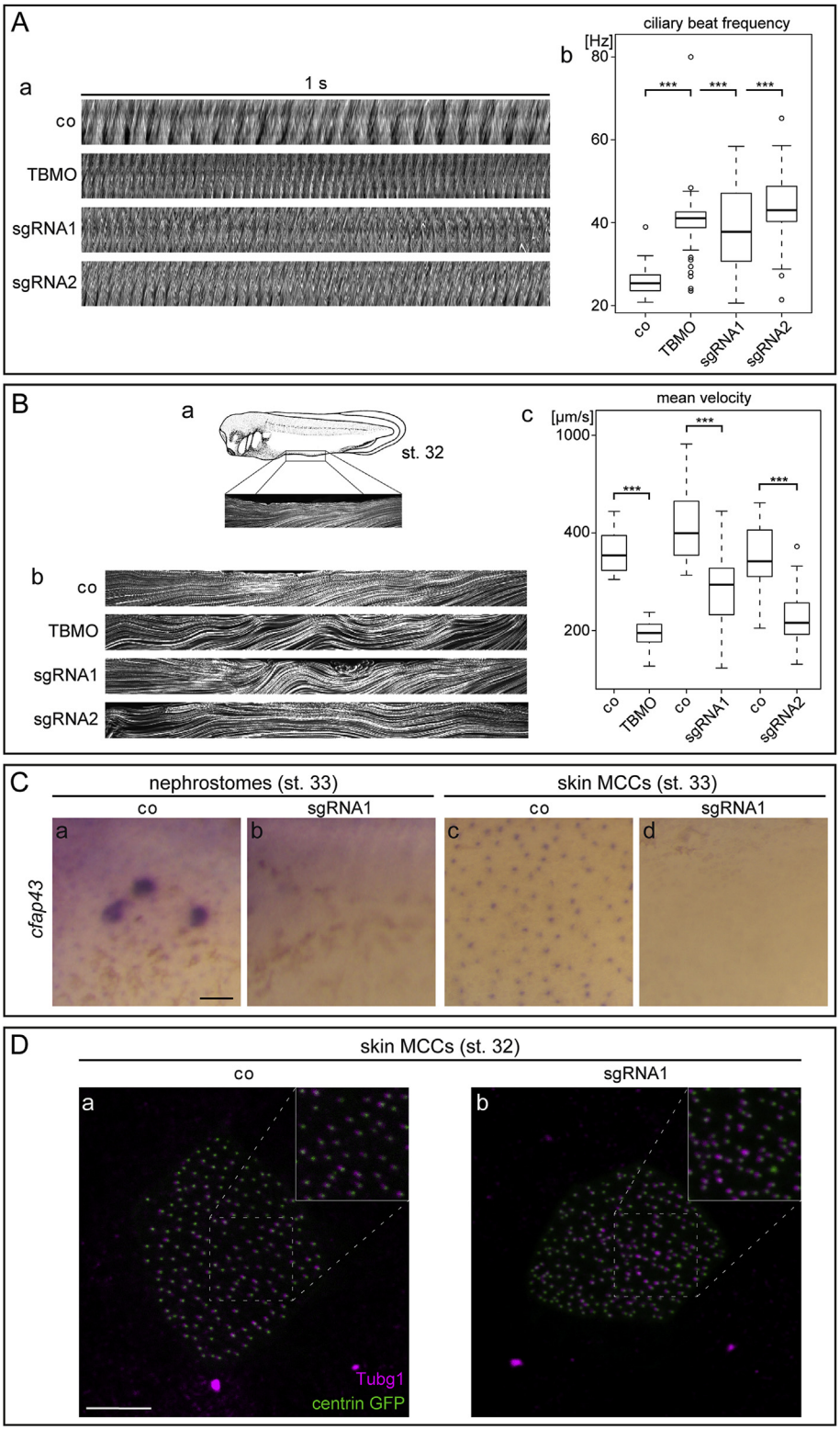

Fig. 4. Ciliary defects in *Xenopus cfap43* morphant and crispant larval skin.
(A) (a) Kymographs of ciliary motility of single MCCs were generated from control (co) wt, TBMO-, sgRNA1-and sgRNA2-injected specimens. (b) Statistical evaluation of results from 3 independent experiments with 15 embryos each and 5 analyzed MCCs per embryo revealed elevated ciliary beat frequencies upon *cfap43* loss-of-function. **(B)** (a) Schematic depiction of the region used for flow analysis in control wt and manipulated stage 32 embryos. Embryo scheme taken from https://www.xenbase.org/anatomy/alldev.do. (b) Maximum intensity projections of single control wt, TBMO-, sgRNA1-and sgRNA2-injected specimens represent cilia-generated flow. (c) Evaluation of bead transport from 3 independent experiments with 8 analyzed specimens each shows reduced mean velocities in *cfap43* morphants and crispants. **(C)** *cfap43* mRNA transcripts were reduced in *cfap43* crispant embryos (b, d) at stage 33, with a focus on nephrostomes (a, b) and MCCs (c, d). Morphant Embryos were injected with 0.5 pmol TBMO. **(D)** IF staining of basal bodies (centrin GFP) and basal feet (Tubg1) in skin MCCs of stage 32 wildtype and crispant specimens. Scale bars: C = 100 µm, D = 10 µm ***, $p<0.001$.

obtained at the expected Mendelian ratio (62 or 28.6% wt, 104 or 47.9% heterozygotes, 51 or 23.5% homozygotes). Except for three mice, which developed a cranial vault around weaning indicative of hydrocephalus, no externally visible abnormalities were detected in >100 adult mutants.

Next, we analyzed the presence or absence of CFAP43 protein in knockout mice. We were unable to isolate sufficient *Cfap43*$^{\Delta ex3/\Delta ex3}$ sperm cells from the cauda epididymis for Western blot analysis, and crude testis lysates gave rise to high background on Western blots. However, immunoprecipitation of CFAP43 from testis lysates detected CFAP43 in wt but failed to detect full length CFAP43 protein in testis lysates of homozygous *Cfap43*$^{\Delta ex3}$ males, using the polyclonal P4 or the monoclonal 27D5 antibody (Fig. 5B). Also, a predicted shorter variant with an apparent molecular weight of 172 kDa, which potentially could result from splicing of exon 2 into exon 7, restoring the reading frame,

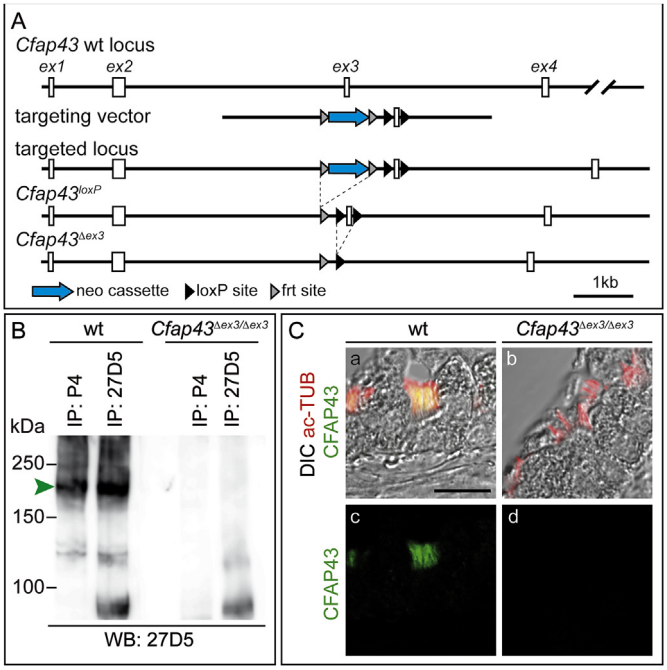

Fig. 5. Generation and validation of a *Cfap43* null allele in the mouse. **(A)** *Cfap43* wt locus, targeting vector, and targeted alleles (*Cfap43* targeted locus, $Cfap43^{loxP}$, and $Cfap43^{\Delta ex3}$). **(B)** Western blot analysis of CFAP43 following IP with polyclonal antibody P4 or MAb 27D5 from testes lysates shows absence of CFAP43 protein in $Cfap43^{\Delta ex3/\Delta ex3}$ mutants. The green arrowhead points to CFAP43 protein. **(C)** Indirect IF staining of lung sections of wt and $Cfap43^{\Delta ex3/\Delta ex3}$ mutants using monoclonal antibody 5B1 co-stained with acetylated α-tubulin (ac-TUB) shows CFAP43 in cilia in wt, but its absence in $Cfap43^{\Delta ex3/\Delta ex3}$ lungs. Full size Western blot for B is shown in Fig. S9C. Scale bar in C = 10 μm.

was not detected (Fig. 5B). Consistently, staining of cilia on epithelial cells lining the airways of the lung was lost in $Cfap43^{\Delta ex3/\Delta ex3}$ mice (Fig. 5C). Deletion of exon 3 thus prevented the translation of CFAP43 protein, indicating that $Cfap43^{\Delta ex3}$ in all likelihood represented a *bona fide* null allele.

Left-right defects were not observed in 21 homozygous $Cfap43^{\Delta ex3}$ mutants, as assessed by the analysis of organ situs, consistent with the results in *Xenopus* morphants and crispants.

Expression in multiciliated cells of the respiratory tract suggested a potential function of CFAP43 for cilia motility and mucociliary clearance. Indeed, mucus accumulation was observed by PAS staining of histological sections in the nasal cavities of three months (n=3) and one year old (n=6) mutant mice (Fig. 6A). Mucus-producing goblet cells were present in equal numbers in wt and *Cfap43* knockout specimens (Fig. S6, Table S3), and CFAP43 was exclusively present on wt airway MCCs (n=3, Fig. 6B), strongly suggesting that mucus accumulation was caused by MCC defects. Analysis of trachea sections of 6–7 weeks old mice showed that cilia on mutant MCCs were present, and marker proteins of outer and inner dynein arms as well as radial spokes were detected as in wt (Fig. 6C). Likewise, TEM analysis of lung sections showed no obvious alterations in axonemal structures or rotational polarization of cilia (Fig. 6D), Additionally, and cilia length was unaltered in isolated $Cfap43^{\Delta ex3}$ mTECs as compared to wt (Fig. 6E). Mutant tracheal MCC cilia were motile and – at first glance – appeared indistinguishable from wt (Movie S4). However, quantitative analyses of ciliary beat frequencies (CBF) in tracheal cilia of 6–9 months old wt and knockout mice, revealed a significant increase in CBF from on average of 10 Hz in wt to about 16 Hz in mutants (Fig. 6Fa, b; Fig. S7; raw data in Table S4). To analyze the functional consequences of altered CBF, fluorescent beads were added to tracheal epithelial explants (Fig. S7C). Despite the increase in CBF, bead transport was markedly reduced in mutant samples (Fig. 6Fc; Movie S5, raw data in Table S5), corroborating the results obtained in frog tadpole skin (cf. Fig. 4A, B; Movies S2, S3).

Supplementary video related to this article can be found at https://doi.org/10.1016/j.ydbio.2019.12.010.

$Cfap43^{\Delta ex3/\Delta ex3}$ females bred and raised their offspring normally, whereas males (n=6) were infertile when mated to wt or mutant females, due to severe sperm defects (Fig. 7A; Movie S6), in agreement with findings in humans (Tang et al., 2017). In correlation with the differentiation of sperm cells during the first round of spermatogenesis, upregulation of *Cfap43* expression was detected starting at d15 (Fig. 7B). *Cfap43* loss in mutant males did not impair the structure of seminiferous tubules and lumina contained sperm cells (Fig. 7Ca, b, e, f). However, flagella were not present in the center of the lumina but appeared dispersed in $Cfap43^{\Delta ex3/\Delta ex3}$ mutants (Fig. 7Ce, f). In the cauda epididymis of mutants, only few tubules were filled with sperm cells as compared to wt (Fig. 7Cc, c', g, g', d, d', h, h'), while tubules themselves appeared normal (Fig. 7Cc, g). In mutant tubules that contained sperm cells, staining of axonemes with acetylated α-Tubulin (ac-TUB) appeared reduced (Fig. 7Cd, d', h, h'). Isolated epididymal sperm cells frequently showed short flagella (442/489) that contained coiled (188/489) or split (80/489) axonemes (Fig. 8B, Table S6). The midpiece was severely shortened, as indicated by localization of mitochondria (visualized by COXIV staining; Fig. 8Ba-c) and position of the annulus (visualized by SEPT7 staining; Fig. 8Bd-f). Fibrous sheath material (visualized by AKAP3 staining) was not associated with microtubules but concentrated between split or coiled axonemes, or was absent (Fig. 8Bg-j).

Supplementary video related to this article can be found at https://doi.org/10.1016/j.ydbio.2019.12.010.

Ultrastructural analysis of $Cfap43^{\Delta ex3/\Delta ex3}$ epididymis sections by transmission electron microscopy (TEM) showed fewer sperm nuclei (red asterisks in Fig. 8Ca, b) and flagellar cross sections (red arrows in Fig. 8Cb) as well as large and partly fragmented cytoplasmic structures (arrowheads in Fig. 8Cb), as compared to wt specimens (Fig. 8Ca). Cross sections of mutant axonemes showed variable but severe axonemal malformations: at the level of the midpiece (indicated by the presence of peripheral mitochondria, yellow triangles in Fig. 8Cc, f), we observed few and abnormally located disorganized microtubules (small red arrows in Fig. 8Cf) and dislocation of outer dense fibers (ODF pink star; large red arrow in Fig. 8Cf). Sections through the principal piece (indicated by the absence of peripheral mitochondria, Fig. 8Cd, e, g-i) showed single (large red arrows in Fig. 8Cg) or fragmented microtubules (small red arrows in Fig. 8Cg). They possibly represented isolated A- and B-tubules of microtubule doublets, rather than intact doublets. Further, mutant sperm displayed supernumerary (or fragmented) ODFs (pink stars, Fig. 8Cg, h), ODFs located peripheral to the fibrous sheath (red arrowhead in Fig. 8Ch), or lacked the fibrous sheath (Fig. 8Ci).

Histological analysis of $Cfap43^{\Delta ex3/\Delta ex3}$ brains (n=11) from mice not displaying external signs of hydrocephalus showed enlarged ventricles in all cases at 6–13 weeks of age (arrowhead in Fig. 9Af). Enlarged ventricles were invariably observed in brains from homozygous mutants at day P7 (n=4/4), P5 (n=3/3) and P3 (4/4), as well as in 3/5 brains analyzed at P1 (Fig. 9Ag-j). Sagittal sections of P5 $Cfap43^{\Delta ex3/\Delta ex3}$ brains (n=5) revealed no evidence for aqueduct obstruction (arrowheads in Fig. 9B; Fig. S8A). Immunofluorescence staining of P7 brain sections detected glutamylated-tubulin (Glu-TUB) in cilia similar to wt (Fig. 9C). In agreement with the observed early onset of dilated ventricles in $Cfap43^{\Delta ex3/\Delta ex3}$ brains at P1, *Cfap43* expression was detected in the ependymal cells lining the lateral and medial walls of the lateral ventricles, in the aqueduct (AQ), and in the choroid plexus (CP) of E16.5 fetuses (Fig. 9D). High-speed video microscopy showed that *Cfap43* mutant ependymal cilia of the lateral walls were motile and moved fluorescent beads at a slightly reduced, though not significantly slower rate compared to wt littermates (Fig. S8B; Movie S7; raw data in Table S7).

Supplementary video related to this article can be found at https://

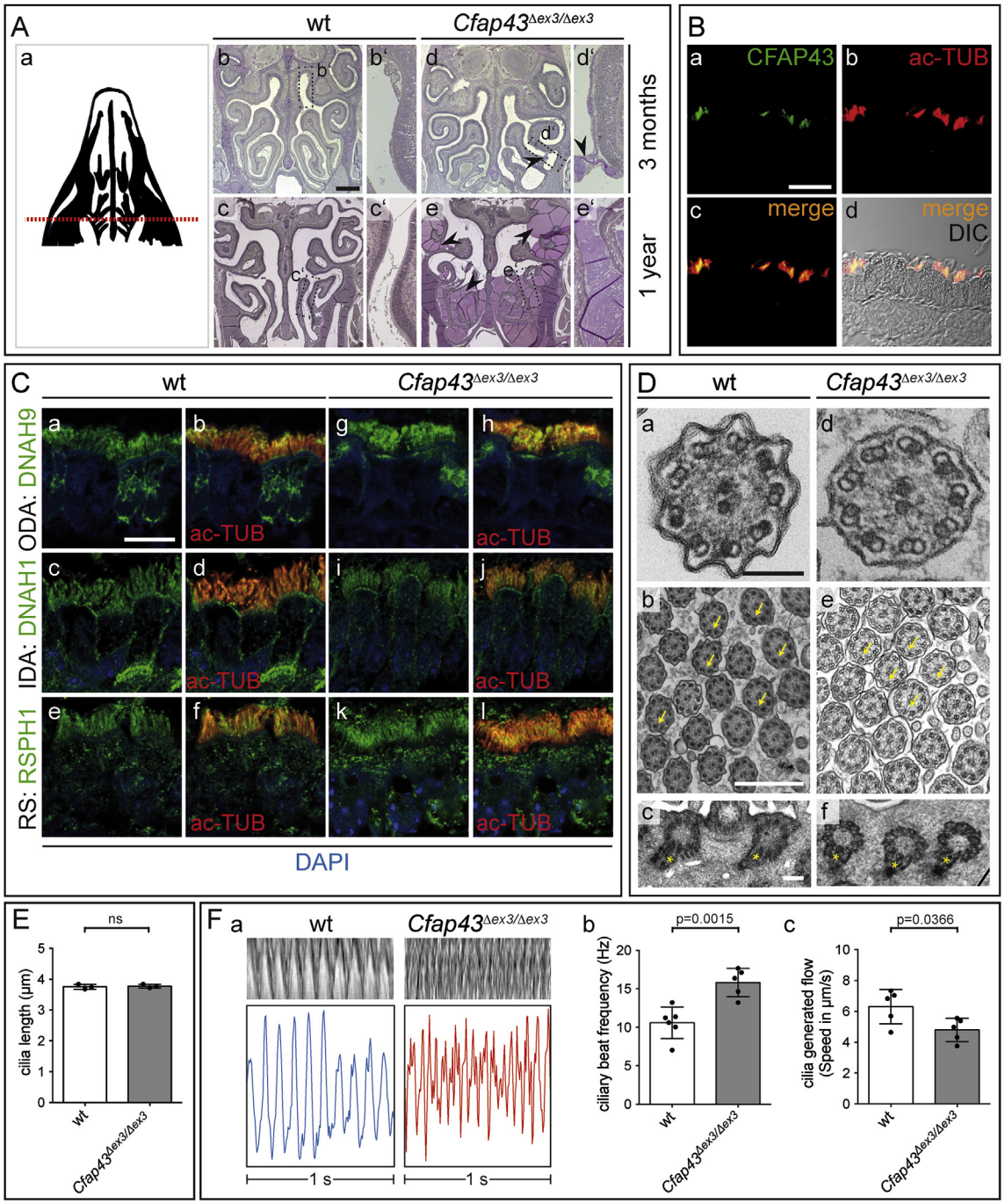

Fig. 6. Airway cilia morphology and function in wt and *Cfap43* knockout mice.
(A) PAS staining of frontal sections (at level indicated in (a)) from nasal cavities of 3 months (b, d) and 1 year (c, e) old wt (b, c) and *Cfap43*$^{\Delta ex3/\Delta ex3}$ (d, e) mice show mucus accumulations in mutants (black arrowheads in (d, e)). Dashed boxes outline areas of higher magnification in (b'-e'). **(B)** IF staining of wt lung sections with monoclonal antibody 5B1 highlights CFAP43 localization exclusively to cilia of epithelial cells, which were co-stained with acetylated α-tubulin (ac-Tub). **(C)** Outer dynein arms (ODA, DNAH9: a, b, g, h), inner dynein arms (IDA, DNAH1: c, d, i, j), and radial spokes (RS, RSPH1: e, f, k, l) are present in wt (a–f) and *Cfap43*$^{\Delta ex3/\Delta ex3}$ (g–l) tracheal cilia. **(D)** TEM analyses of wt (a–c) and *Cfap43*$^{\Delta ex3/\Delta ex3}$ (d–f) lung cilia axonemes demonstrate normal arrangement of 9 + 2 axonemes (a, d) and normal rotational polarization of cilia, as indicated by orientation of central microtubule pairs (yellow arrows in b and e) and basal feet (yellow asterisks in c and f). **(E)** Cilia length is comparable in wt and *Cfap43*$^{\Delta ex3/\Delta ex3}$ tracheas. Each dot represents the average cilia length from one individual. **(F)** (a) Representative kymographs (above) and plotted values (bellow) of wt (blue) and *Cfap43*$^{\Delta ex3/\Delta ex3}$ (red) tracheal cilia motility (t = 1 s) depict ciliary beat frequency (CBF). (b) CBF is enhanced in *Cfap43*$^{\Delta ex3/\Delta ex3}$ as compared to wt tracheal cilia. Each dot represents the average CBF of one specimen (n≥11 cells analyzed). (c) Cilia generated flow is reduced in *Cfap43*$^{\Delta ex3/\Delta ex3}$ versus wt tracheas. Each dot represents the average ciliary flow per specimen from n≥3 recordings. More details concerning CBF and ciliary flow measurement are shown in Fig. S7. Scale bars: A = 1 mm; B = 20 µm; C = 10 µm; Da, d = 100 nm; Db, e = 500 nm; Dc, f = 100 nm.

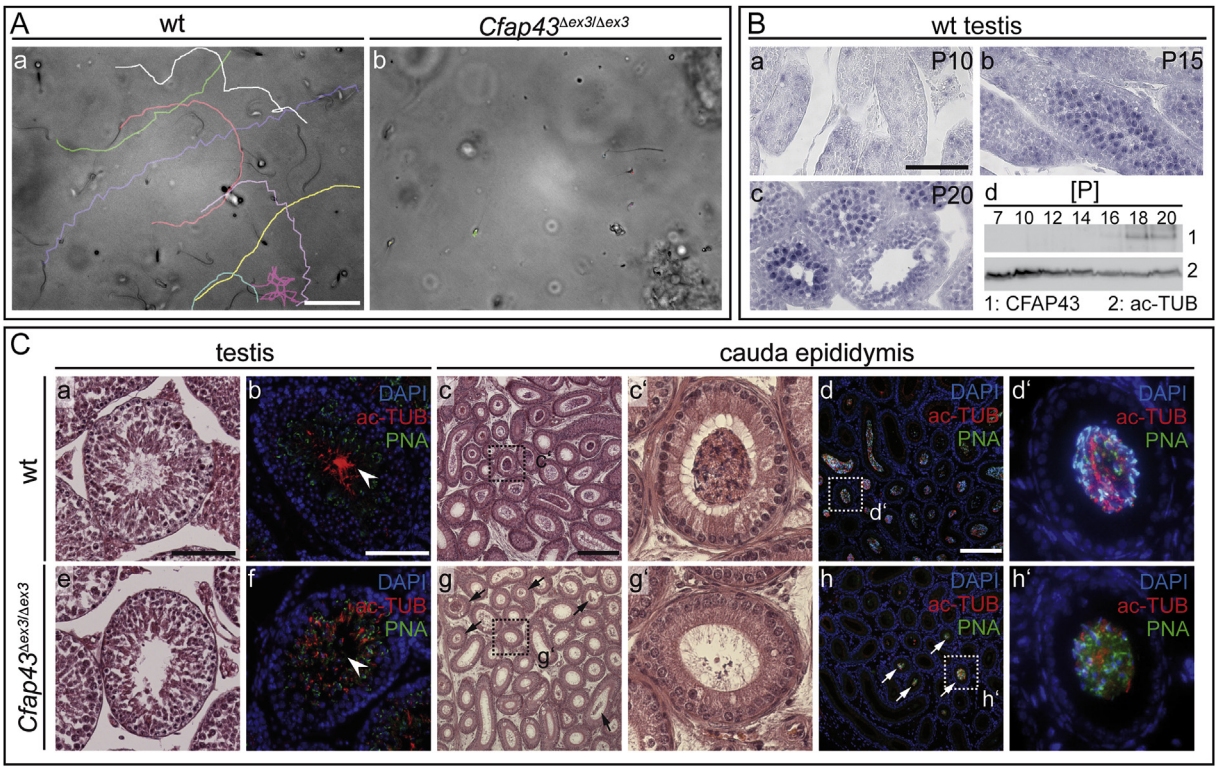

Fig. 7. *Cfap43* expression during spermiogenesis and sperm defects in *Cfap43*$^{\Delta ex3/\Delta ex3}$ males.
(A) Representative trajectories of wt and *Cfap43*$^{\Delta ex3/\Delta ex3}$ sperm motility reveal immobility of sperm from mutant mice (cf. Movie S6). **(B)** SISH on wt testis (a–c) and WB analysis of wt testis lysates (d) show upregulation of *Cfap43* expression from postnatal (P) day P15 on. Full size Western blot is shown in Fig. S9D. **(C)** Histological (HE) (a, c, c', e, g, g') and immunostained (b, f, d, d', h, h') sections show wt (a-d') and *Cfap43*$^{\Delta ex3/\Delta ex3}$ (e-h') testes (a, b, e, f) and cauda epididymides (c-d', g-h'). In immunostainings the acrosome was marked by PNA (green) and the sperm flagella were labelled using acetylated α-tubulin (ac-TUB, red). DAPI was used to stain nuclei (blue). Scale bars: A = 50 μm, Ba-c = 100 μm; Ca, b, e, f = 100 μm; Cc, d, g, h = 200 μm.

doi.org/10.1016/j.ydbio.2019.12.010.

In summary, our analyses of *Cfap43* null mutant mice demonstrated that CFAP43 function was not limited to sperm flagella, but also required in airway epithelia and brain ependyma, tissues carrying and requiring motile cilia function.

3. Discussion

Originally, we identified *Cfap43* as a gene acting downstream of FOXJ1 in the fetal respiratory epithelium of the mouse lung (Stauber et al., 2017). The conserved nature of this regulation became obvious in wt *Xenopus* embryos, where both genes were largely co-expressed, as well as in gain- and loss-of-function scenarios. In the mouse, *Cfap43* expression was consistently reduced in epithelial cells lining the large airways of the lung, and absent in ependymal cells and the choroid plexus of *Foxj1*$^{-/-}$ fetuses (Fig. 1E). Surprisingly, however, *Cfap43* expression was unaffected in the upper respiratory tract of mouse *Foxj1*$^{-/-}$ knockout specimens and only moderately reduced at the frog larval proctodeum (Fig. 2C), suggesting differential regulation of *Cfap43* in the various cell populations carrying motile cilia. Members of the RFX family of transcription factors can act downstream (ventral node; Alten et al., 2012) or upstream (ependymal cells; Zein et al., 2009) of FOXJ1, or in a redundant manner (floor plate; Cruz et al., 2010); they might therefore contribute to tissue-dependent differences of *Cfap43* transcription in *Foxj1* mutants. However, in MCCs RFX proteins rather act as scaffolding proteins (Quigley and Kintner, 2017), suggesting that additional tissue-specific factors maintain *Cfap43* transcription in the absence of FOXJ1.

As an evolutionarily highly conserved component of motile cilia, *Cfap43* has been studied before in humans, mice, trypanosomes, and the single-cell green algae *Chlamydomonas reinhardtii*. In humans, mutations in *CFAP43* were causative for a rare type of male infertility, namely MMAF (multiple morphological abnormalities of the sperm flagella). No additional health problems were reported in sterile male patients (Coutton et al., 2018; Sha et al., 2017; Tang et al., 2017). Likewise, no cilia-related defects other than sperm flagellum malformation were reported for the *Cfap43* mutant mice generated by Tang et al. (2017) and Coutton et al. (2018). The null allele that we created in the mouse confirmed both human and mouse sperm phenotypes: sperm were immobile and the morphological and ultrastructural flagella defects observed in patients (Coutton et al., 2018; Sha et al., 2017; Tang et al., 2017) were highly similar to malformations described here. Therefore, the human mutations, which resulted in premature stop codons and splicing defects, likely represent null alleles as well. During spermatogenesis, the material for outer dense fibers and the fibrous sheath is transported along the growing axoneme (Irons and Clermont, 1982a, 1982b), which could explain the mis-arranged accessory structures of the flagellum after loss of CFAP43. Since the flagella appeared distorted in the seminiferous tubules of the testis, defects likely occurred during axoneme formation and were not acquired during later stages of spermatogenesis or in the maturation process. Whether sperm defects arise in frogs as well was not addressed, as raising sexually mature adult frogs is time-consuming. We would, however, anticipate that CFAP43 is required for sperm flagella formation throughout the vertebrates.

Our descriptive and functional investigation of mucociliary epithelia in postnatal mutant mouse and embryonic frog morphant and crispant specimens uncovered a novel function of CFAP43 in motile cilia. Mucus accumulation, as found in *Cfap43* knockout mice, can be caused by alterations of ciliary structure or beating. Ciliary length and rotational polarity, as well as mucus production (inferred from the unchanged number of mucus-producing cells) were apparently not affected by loss of *Cfap43*. However, loss of CFAP43 increased the ciliary beat frequency (CBF) which was accompanied by reduced velocity of cilia generated

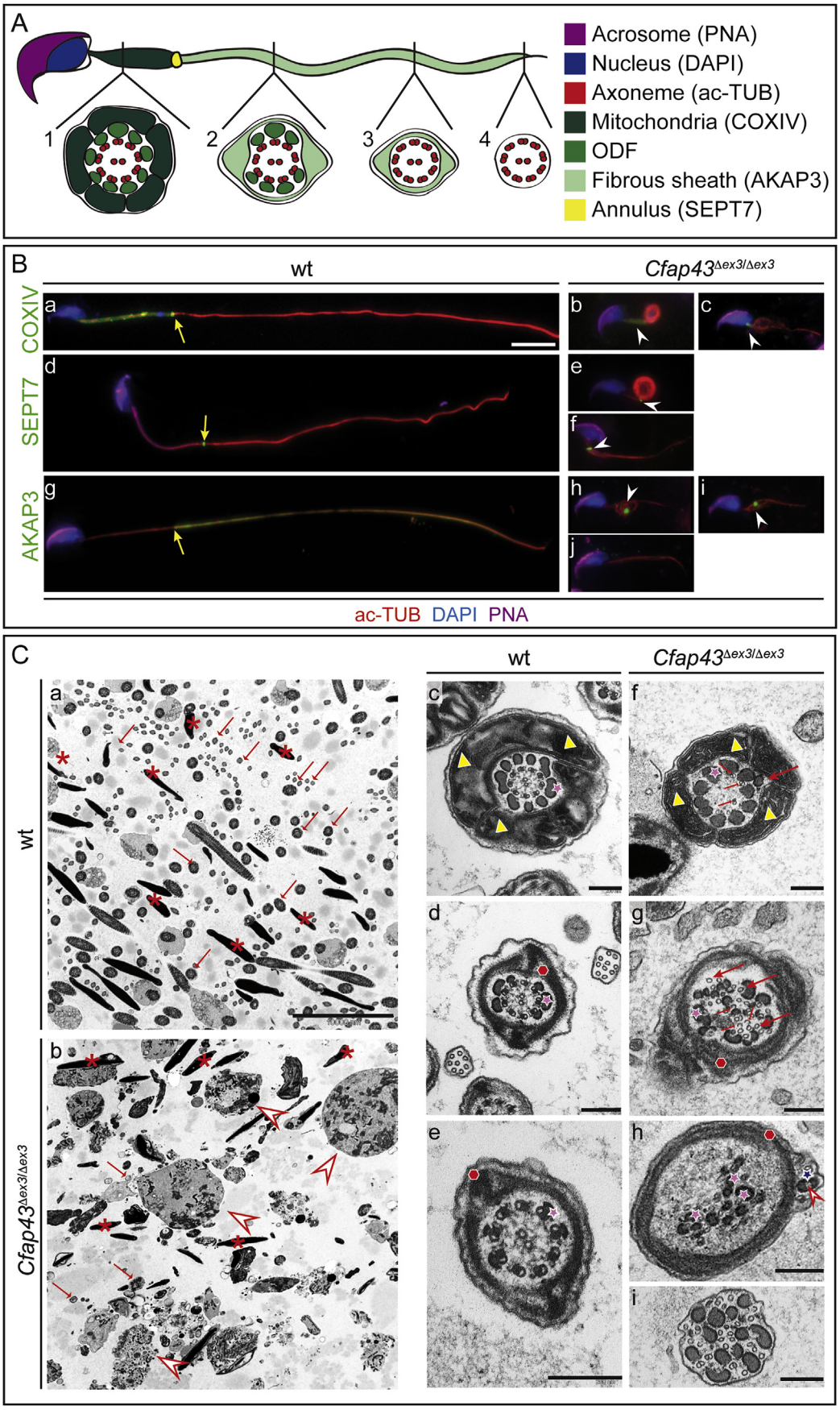

Fig. 8. Subcellular and electron microscopic analysis of *Cfap43*$^{\Delta ex3/\Delta ex3}$ mouse sperm.

(A) Schematic overview indicating the sperm architecture. In the midpiece (1) the axoneme is surrounded by outer dense fibers (ODF) and mitochondria. The annulus is located at the border between the midpiece and the principal piece (yellow). ODFs are continuing in the principal piece (2), surrounded by the fibrous sheath. In the proximal part (3) of the principal piece the ODFs are discontinuous. In the end piece (4) only the axoneme is maintained. **(B)** Characterization of cauda sperm from wt (a, d, g) and *Cfap43*$^{\Delta ex3/\Delta ex3}$ (b, c, e, f, h-j) males. Mutant sperms show a shortened midpiece and malformed axoneme. Axonemes were stained for acetylated α-tubulin (ac-TUB, red), nuclei were visualized using DAPI (blue), and acrosomes were marked by PNA (purple). (a–c) Mitochondria are shown by COXVI (green). (d–f) The annulus is marked by SEPT7 (green). (g–j) AKAP3 was stained to highlight fibrous sheath (green). Yellow arrows point to midpiece/principal piece border in wt; white arrowheads point to shortened midpiece region containing mitochondria in (b, c), to annuli abnormally close to the sperm head in (e, f) of *Cfap43*$^{\Delta ex3/\Delta ex3}$ mutant sperm, and to abnormal localization of fibrous sheath material between coiled or split axonemes close to the sperm head (h, i). In some cases no fibrous sheath was detected in *Cfap43*$^{\Delta ex3/\Delta ex3}$ mutant sperm (j). **(C)** Overviews of wt (a) and *Cfap43*$^{\Delta ex3/\Delta ex3}$ (b) sections show large, partly fragmented cytoplasmic structures in *Cfap43*$^{\Delta ex3/\Delta ex3}$ (b, arrowheads). Red asterisks indicate sperm heads, red small arrows point to flagellar cross sections. (c, f) Detail images show flagellar cross sections of wt (c) and *Cfap43*$^{\Delta ex3/\Delta ex3}$ (f) sperms at the midpiece level as indicated by the presence of peripheral mitochondria (yellow triangles). Pink stars mark outer dense fibers (ODFs); the large red arrow points to a dislocated ODF; small red arrows point to abnormally located microtubules. (d-e, g-i) Detail images show flagellar cross sections of wt (d, e) and *Cfap43*$^{\Delta ex3/\Delta ex3}$ (g–i) principal pieces as indicated by the absence of mitochondria and the presence of fibrous sheath (red hexagons). (h) Arrowhead points to ODFs (blue star) peripheral to the fibrous sheath. (i) Detail image of flagellar principle piece cross section of *Cfap43*$^{\Delta ex3/\Delta ex3}$ lacking fibrous sheath material. Scale bars: B = 10 μm; Ca, b = 10 μm; Cc-h = 200 nm.

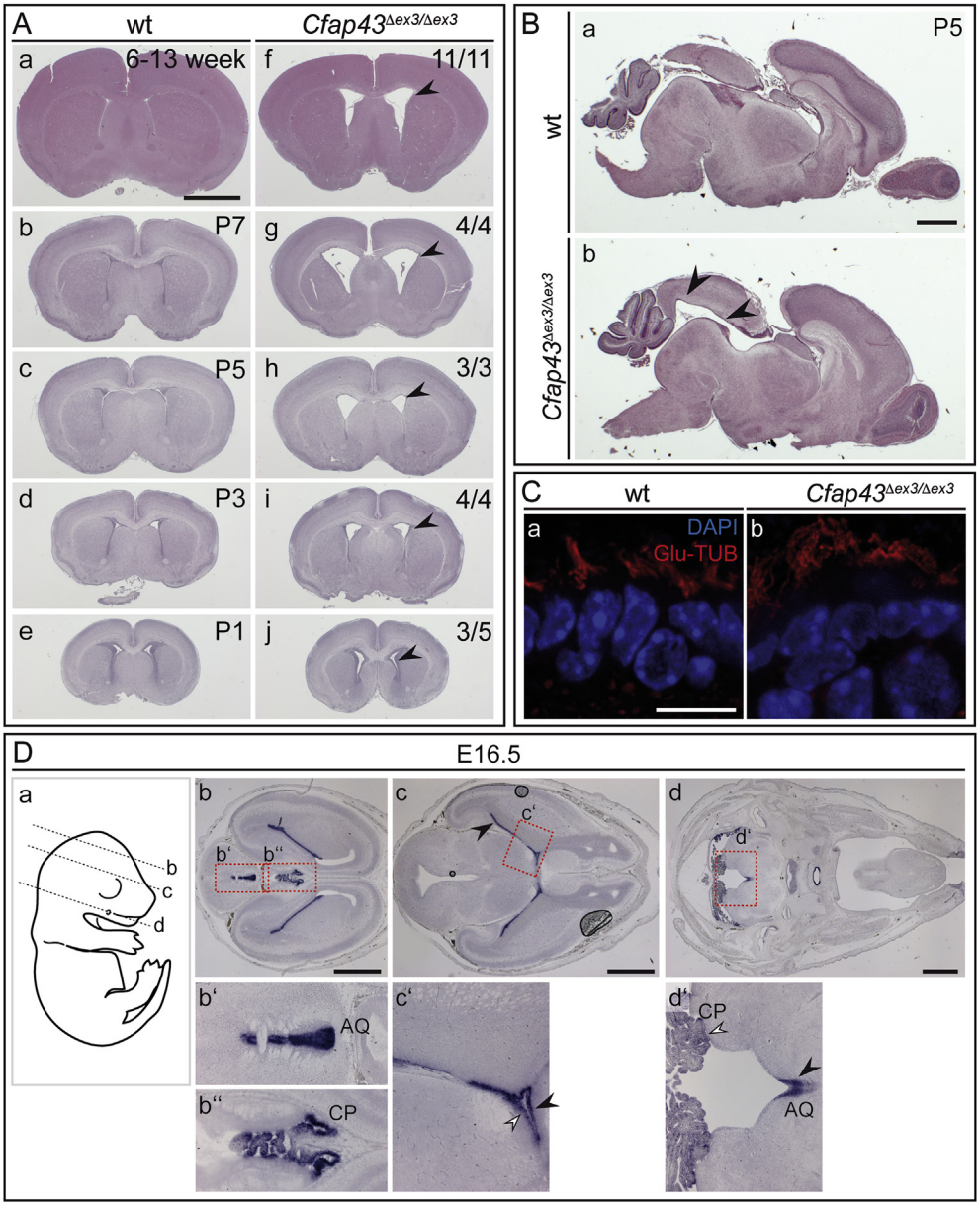

Fig. 9. Brain defects in *Cfap43*$^{\Delta ex3/\Delta ex3}$ mouse mutants.
(A) HE stained frontal sections of wt (a–e) and *Cfap43*$^{\Delta ex3/\Delta ex3}$ (f–j) mouse brains at different postnatal days show dilated ventricles (arrowheads) in mutant mice. **(B)** Midsagittal sections of P5 wt (a) and *Cfap43*$^{\Delta ex3/\Delta ex3}$ (b) mouse brains show no obstruction of the aqueduct (arrowheads). **(C)** Ependymal cilia are present in P7, as demonstrated by IF staining of brain sections for glutamylated-tubulin (Glu-TUB, red) in wt (a) and *Cfap43*$^{\Delta ex3/\Delta ex3}$ (b) mouse brains. Nuclei are marked by DAPI staining (blue). **(D)** (b–d) *Cfap43* transcripts are expressed in mouse embryonic brain at E16.5. SISH of transverse sections (section planes are indicated in a); red boxes are magnified in b', b'', c' and d'. Black arrowheads in (c) and (c') point to *Cfap43* expression in the lateral wall of the lateral ventricles, white arrowhead in (c') highlights expression at the medial wall. Black arrowhead in (d') points to *Cfap43* expression in the AQ, white arrowhead in (d') highlights *Cfap43* expression in the CP of the fourth ventricle. AQ: aqueduct; CP: choroid plexus. Scale bars: A = 2 mm; B = 1 mm; C =10 μm; D = 1 mm.

flow (CGF). Such an - at first glance - counter-intuitive observation is not unprecedented and was for example also found in knockout mice of *Ttll1*, a gene encoding a tubulin glutamylating enzyme (Ikegami et al., 2010). *Ttll1* mutant cilia were characterized by a loss of beating asymmetry, i.e. the velocities of the effective (transport of mucus) and recovery stroke (restoring the initial position) where similar (Ikegami et al., 2010). Reduced CGF in *Cfap43*-mutant tracheal cells, despite increased CBF, could therefore be caused by alterations of velocities of effective or recovery stroke, changes in wave form or ciliary bending, parameters that we could not resolve in our analyses. The observed mucus accumulation in the upper airways of mutant mice likely arise as a consequence of this defect. Incidentally, *Ttll1* knockout mice displayed mucociliary clearance defects as well (Ikegami et al., 2010). The larval skin of the frog tadpole did not show mucus accumulation, most likely because the mucociliary epithelium exists only for a short interval of about three days (roughly stages 20–40). Mucociliary defects in human patients were not reported, but may have gone unnoticed.

Our reasoning that CFAP43 impacts on ciliary motility in a rather subtle way is further supported by analyses of the CFAP43 orthologues FAP43 in *Tetrahymena* and *Chlamydomonas*. In both organisms, FAP43 is a component of the tether/tether head complex that together with FAP44 links the inner dynein arm (IDA) subspecies f (I1 dynein) motor head to the A-tubule of the outer microtubule doublet (Fu et al., 2018; Kubo et al., 2018; Urbanska et al., 2018). The two-headed IDA I1 has been suggested to impact on the wave form through modulation of cilia bending, rather than on microtubule sliding (Kubo et al., 2018; Urbanska et al., 2018). In *Tetrahymena*, loss of FAP43 affected the ciliary wave form, beat stroke and swimming velocity (Urbanska et al., 2018), whereas subtle flagellar beating defects were seen upon loss of FAP43 in *Chlamydomonas* (Kubo et al., 2018). Using STED microscopy and immunogold labelling, tagged CFAP43 was located between the axoneme and paraflagellar rod of *T. brucei* (Coutton et al., 2018). An evolutionary conserved localization of CFAP43 (together with CFAP44) to a bridge between axonemal microtubule doublets 5 and 6 was proposed and discussed to restrict ciliary and flagellar movement to a planar beating form (Afzelius, 1959; Lin et al., 2012; Lindemann et al., 1992). Further studies and improved tools to analyze, dissect and describe ciliary beating of airway epithelial and ependymal cells are needed to unravel the functional consequences of CFAP43 loss for the wave form of cilia on multiciliated cells in vertebrates. Likewise, further studies will be

required to elucidate the biochemical function of CFAP43. Towards this aim we identified potential interaction partners by immunoprecipitation of CFAP43 from adult mouse testes and subsequent mass spectrometric analysis, which led to a number of candidate proteins (Table S8) that, when validated, should provide entry points for further biochemical analyses.

Most *Cfap43* mutant mice showed dilated ventricles at P1, before full maturation of ependymal epithelia, but after onset of multiciliogenesis on the ventromedial wall of the lateral ventricles (Abdelhamed et al., 2018; Ibañez-Tallon et al., 2004). The observed phenotype was fully penetrant by P7, concomitant with the maturation of ependymal cilia, but progressed only in rare cases to externally visible hydrocephalus. Therefore, the detected hydrocephalus upon loss of CFAP43 in mice may be caused by early defects in choroid plexus cilia (Banizs et al., 2005), medial wall cilia (Abdelhamed et al., 2018), impaired ependyma, or a combination thereof. Ependymal cilia were motile both in mouse and frog, and ependymal flow in mouse brains was apparently unaltered. Recently, a heterozygous mutation in *Cfap43* was described in a Japanese family with normal pressure hydrocephalus (NPH) (Morimoto et al., 2019). NPH constitutes a variant of hydrocephalus that develops past the age of 40 and is characterized by excess cerebrospinal fluid production. However, the progression of NPH contrasts with the early-onset hydrocephalus found in our knockout mice. In-depth studies, beyond the scope of the present investigation, are needed to unravel the molecular mechanism of hydrocephalus formation in mutant mice. It is tempting to speculate, however, that a choroid plexus ciliary defect results in excess CF, which causes early onset hydrocephalus in mouse and NPH in humans, although the presumed dominant-negative mode of action of the described human mutation (Morimoto et al., 2019) needs to be confirmed and mechanistically evaluated. The lack of hydrocephalus in mutant frog embryos may be due to the much earlier time point of analysis, before the onset of metamorphosis. It may be worthwhile to generate a mutant line in *Xenopus tropicalis*, in order to assess *cfap43* function in the developing and adult brain, with a focus on CF production in the choroid plexus.

Male infertility, mucociliary clearance defects of the airways, and hydrocephalus are hallmarks of primary ciliary dyskinesia (PCD) in humans and mouse models of this disease. In that sense, the knockout mouse fulfils some criteria of PCD. PCD patients generally are characterized by immobile cilia. *Cfap43*, therefore, does not qualify as a PCD gene. Also, besides infertility, no other defects have been described in human male MMAF patients. It may, however, be useful to re-evaluate patients for NPH and subtle mucociliary clearance defects. If such pathologies were detected, *Cfap43* may represent a gene for a PCD subtype that accounts for more subtle phenotypes.

4. Conclusions

CFAP43 is a highly conserved axonemal protein of motile cilia. Besides the known function in mammalian sperm cells, CFAP43 is required in the brain and respiratory tract of mice, as well as in skin MCCs in frog embryos. Airway mucus accumulation in mice occurs most likely due to changed beating of multiciliated epithelial cells of the respiratory tract leading to reduced velocity of the generated mucus flow. Changes in the ependymal flow were not observed as a cause for hydrocephalus formation, suggesting that more subtle ciliary or other defects underlie the development of this phenotype.

5. Materials and methods

Multiple protein sequence alignment: Sequences were aligned using ClustalW (v1.83; multiple sequence alignment; Pairwise Alignment Mode: Slow; Pairwise Alignment Parameters: Open Gap Penalty = 10.0, Extend Gap Penalty = 0.1, Similarity Matrix: gonnet; Multiple Alignment Parameters: Open Gap Penalty = 10.0, Extend Gap Penalty = 0.2, Delay Divergent = 30%, Gap Distance = 4; Similarity Matrix: gonnet).

Ethics approval: Animals were handled in accordance with the German regulations (Tierschutzgesetz) and for mice approved by the ethics committee of Lower Saxony for care and use of laboratory animals (LAVES, Niedersächsisches Landesamt für Verbraucherschutz und Lebensmittelsicherheit), for frogs by the Regional Government Stuttgart, Germany (A379/12 Zo 'Molekulare Embryologie'). Mice were kept in the central animal facility of Hannover Medical School (ZTL) and maintained as approved by the responsible Veterinary Officer of the City of Hannover.

5.1. Mouse methods

Experimental animals: Cfap43 mutant mice were generated and genotyped as described below. Other mouse lines used were described previously: *Foxj1* mutants (*Foxj1*^{lacZ}) (Brody et al., 2000), Zp3:Cre (de Vries et al., 2000), and FLPe (Rodríguez et al., 2000).

Generation of a conditional Cfap43 allele: A targeting vector containing exon 3 flanked by loxP sites and approximately 1 kb of intron 2 and 3, respectively, and a neomycin resistance cassette flanked by frt sites inserted upstream of exon 3 was generated by standard cloning procedures. Linearized targeting vector DNA and CRISPR-Cas plasmid pX330 (Cong et al., 2013) containing the guide sequence 5′-GTCAT CTGGATGTGACAGTCC-3′ were introduced into ES cells by electroporation. ES cells were screened for homologous recombination by PCR using the following primer pairs: 5'flank: (5'-AAGTACGAGAAGGAGGT AGTAAGGC-3′, 5′-GGCTGGACGTAAACTCCTCTTCAGA-3′); 3′flank: (5′-GAGATTGGAAAACATTTTACCAGTGAAGT-3′, 5′-GAGATTGGAAAA CATTTTACCAGTGAAGT-3′). The presence of both loxP sites in positive clones was ascertained using primer pairs (5′-AATAGCAGG-CATGCTGGGGATG, GGGACTTACCAGAGGGCCAGC-3′) and (5′-GGATC CGACAGTCCTGGATTGTGTCTT-3′, 5′-GAAAGTTAACCTTCCCATCAT CCCCTG-3′), respectively. PCR positive clones were further characterized by Southern blot hybridization. Southern probes were generated from genomic DNA (5′ probe: genomic *Cfap43* DNA from bp 4149–5325 (start ATG set as bp 1); primers: 5′-AAGTACGAGAAGGAGGTAGTAAGGC-3′, 5′-TAGATCACACGAAGTGTTCTGTCC-3'; 3′ probe: genomic DNA from bp 8636–9203, primers 5′-TAAATAAGGATTGCGATCTTTTTAGGA-3′, 5′-GGCCATGGGGTCTGCTCAC-3′) and labelled using Prime-It II Random primer labelling kit (Agilent). Southern blotting and hybridization were performed following standard procedures. Correctly targeted ES-cells were injected into CD1 morulae or blastocysts. The neomycin cassette of mutant mice was excised by breeding with FLPe mice (Rodríguez et al., 2000), and exon 3 was excised by crossing with ZP3:Cre mice (de Vries et al., 2000). Mice resulting from integration of the targeting construct were genotyped by PCR using primers 5′-GCTCTATG GCTTCTGAGGCGG-3′ and 5′-GGGACTTACCAGAGGGCCAGC-3' (mutant product 291 bp, no wt product), and mice containing floxed *Cfap43* exon 3 (*Cfap43*^{loxP}) without the neomycin cassette were genotyped using primers 5′-TCACCCGGCCTCCCCAAG-3′ and 5′-TCCAGGACTGTCG-GATCCACCT-3' (mutant product 687 bp, wt product 602 bp). *Cfap43*$^{\Delta ex3}$ mice were genotyped using primers 5′-GCCAGTCACTAGGG AAAGGGAAGC-3′ and 5′-TCCGGTGAAACCAGGGGTCAG-3′, which give rise to a 271 bp wt and a 193 bp mutant product, respectively.

Collection, embedding, and sectioning of mouse tissues: For tissue collection mice were killed by cervical dislocation. Tissues were dissected, fixed overnight at 4 °C in 4% PFA or 100% methanol, if necessary decalcified in 0.5 M EDTA for 2 weeks exchanging EDTA every other day, dehydrated, and embedded in paraffin according to standard procedures. Embedded tissues were sectioned at 5 or 10 μm.

Transmission electron microscopy (TEM): Epididymides and lungs were dissected from 3-month-old wt and *Cfap43*$^{\Delta ex3/\Delta ex3}$ littermates. Tissues were fixed, embedded, and analyzed as previously described (Rudat et al., 2014).

Section in situ hybridizations (SISH): SISH were performed on 10 μm sections of PFA fixed and paraffin-embedded tissues as described in Moorman et al. (2001). DIG-labelled RNA probe was produced from

FANTOM plasmid PX00616F12 (Kawai and Hayashizaki, 2003) using the Roche DIG RNA labelling system.

Whole mount in situ hybridization (WISH): WISH were performed on E8.25 old embryos as described in (Stauber et al., 2017). DIG-labelled RNA probe was produced from FANTOM plasmid PX00616F12 (Kawai and Hayashizaki, 2003) using the Roche DIG RNA labelling system.

Histology on tissue sections: Histological staining was performed on 10 μm sections of PFA fixed and paraffin-embedded tissues. Hematoxylin and eosin (HE) staining was performed according to standard procedures. PAS staining was carried out using the Periodic Acid-Schiff (PAS) Kit (Sigma Aldrich) according to manufacturer's instructions.

Isolation and processing of sperm cells: For isolation of sperm, epididymides were collected and cut into 1–3 mm fragments in HTF medium (101.65 mM NaCl, 4.7 mM KCl, 199.5 μM $MgSO_4$, 370.5 μM KH_2PO_4, 25 mM $NaHCO_3$, 2.7 mM $CaCl_2$, 2.8 mM glucose, 0.33 mM sodium pyruvate, 18.3 mM sodium lactate, Pen/Strep, 0.0002% phenol red, 4 mg/ml BSA) containing 0.5% methyl-cellulose for video-microscopy or PBS for other applications, and shaken 15 min at 600 rpm. For video-microscopy, sperm was incubated in HTF for 1 h before documentation. Sperm cells in PBS were spread on glass slides and dried before further processing.

Isolation of murine tracheal epithelial cells (mTECs): Multiciliated cells of the airways were collected by tracheal brushing, suspended in PBS, spread on glass slides, and air-dried before further processing.

Cell culture: L-cells allowing for inducible CFAP43 expression under control of the Tet ON/OFF system (Clontech) were maintained in DMEM/F12 (Gibco) containing 10% FCS, Pen/Strep, and 2 mM Glutamax. For induction of CFAP43 expression, 1 μg/ml doxycycline was added to the medium for 24 h. Murine tracheal epithelial cells (mTECs) were isolated and cultured at air liquid interface (ALI) as described in (You and Brody, 2013). CHO cells were cultured in DMEM/F12 containing 10% FCS, Pen/Strep, and 2 mM Glutamax (Gibco). Transfections were performed using Perfectin (Genlantis) according to manufacturer's instructions.

RNA isolation and RT-PCR: RNA was isolated using TriReagent (Geyer), cDNA was produced using the Superscript-II Reverse Transcriptase kit (Thermo Fisher Scientific), and PCRs were performed using the Expand High Fidelity PCR system (Roche) using the following primer combinations: mouse *Hprt* (5′-GCTGGTGAAAAGGACCTCT-3'; 5′-CACAGGACTAGAACACCTGC-3′), mouse *Cfap43* (5′-TCTACGGGAAGAACTGGTGG-3'; 5′-AGCTTGCTGCTTGGAGATGT-3′), mouse *Foxj1* (5′-CTTCTGCTACTTCCGCCATGC-3'; 5′-TCCTCCTGGGTCAGCAGTAAGG-3′).

Generation of antibodies: The rabbit polyclonal antibody against epitope CEKIARERYDNQLKQ (P4) was generated by Biogenes (BioGenes GmbH, Berlin) and affinity purified using P4-coupled SulfoLink Coupling Gel columns (Pierce). Monoclonal antibodies against CFAP43 were generated by immunization of rats and mice with a fragment of CFAP43 containing amino acids 1053–1226 expressed as MBP fusion protein (MBP-CFAP43) in bacteria. MBP-CFAP43 mainly remained in the insoluble fraction of harvested bacteria, thus inclusion bodies were purified as described (O'Callaghan et al., 1998). Insoluble inclusion bodies were resuspended in PBS and 50 μg were injected intraperitoneally (i.p.) and subcutaneously (s.c.) into LOU/C rats or C57/BL6 mice using incomplete Freund's adjuvant supplemented with 5 nmol CpG 2006 (rats) or CpG 1668 (mice, TIB MOLBIOL, Berlin, Germany). After a six-week interval, a final boost with 50 μg MBP-CFAP43 and CpG was injected i.p. and s.c. three days before fusion. Fusion of the myeloma cell line P3X63.Ag8.653 with the immune spleen cells was performed according to standard procedures. Hybridoma supernatants were tested in a solid-phase immunoassay with MBP-CFAP43 or an irrelevant maltose binding protein coated to ELISA plates. Antibodies from tissue culture supernatant bound to the ELISA plates were detected with HRP conjugated mAbs against the rat IgG isotypes (TIB173 IgG2a, TIB174 IgG2b, TIB170 IgG1 all from ATCC, R-2c IgG2c homemade), thus avoiding mAbs of IgM class. HRP was visualized with ready to use TMB (1-StepTM Ultra TMB-ELISA, Thermo). MAbs that reacted specifically with CFAP43 were further analyzed by Western blots and indirect immunofluorescence. Anti-CFAP43 22A11 (rat IgG2b), anti-CFAP43 5B1 (rat IgG2b), and anti-CFAP43 27D5 (mouse IgG2b) were used in this study.

Immunofluorescence staining: Paraffin sections were deparaffinized, rehydrated and antigens were unmasked by 20 min boiling in 10 mM Tris-HCl pH 9.5, 1 mM EDTA. Dried sperm and tracheal cells were washed in PBS. Unspecific binding was blocked by 5% FCS in PBS. Primary antibodies were incubated at 4 °C overnight, secondary antibodies for 1 h at room temperature. For lung sections primary antibodies were incubated sequentially: First anti-CFAP43 1B5 (overnight at 4 °C), followed by anti-acetylated α-tubulin (1 h at room temperature). Antibodies were diluted in blocking solution: anti-acetylated α-tubulin (ac-TUB) (axoneme, Sigma Aldrich T6793) 1:1000, anti-CFAP43 (22A11) 1:50, anti-CFAP43 (5B1) 1:5, anti-AKAP3 (fibrous sheath, Proteintech 13,907-1-AP) 1:200, anti-CoxIV (mitochondria, Abcam ab202554) 1:200, anti-Septin7 (annulus, IBL international #18991) 1:200, anti-glutamylated-tubulin (Glu-TUB) (AdipoGen AG-20B-0020-C100) 1:500, anti-mouse-Alexa555 (Invitrogen A21424) 1:500, anti-rat-Alexa488 (Invitrogen A11006) 1:500, and anti-rabbit-Alexa488 (Invitrogen A11034) 1:500. DAPI (1 μg/ml, Applichem) and PNA-lectin Alexa467 (2 μg/ml, Thermo Fisher L32460) were incubated together with secondary antibodies.

Immunoprecipitation (IP): For immunoprecipitation, 1 testis was lysed in 1 ml lysis buffer (50 mM Tris-HCl pH 7.5, 500 mM NaCl, 5 mM EDTA, 0.05% NonidetP40, Roche Complete protease inhibitor, and 0.1% BSA), sonicated, debris pelleted at 800×*g* for 10–20 min, and the supernatant was transferred into fresh tubes. Half a testis was used for each IP. 25 μl washed UltraLink beads (Perbio) and anti-CFAP43 antibodies (10 μl P4 or 500 μl 27D5) were added and incubated for 4h at 4 °C. Subsequently, beads were washed 3 times for 20 min in wash buffer (50 mM Tris pH 8.5, 500 mM NaCl, 5 mM EDTA, 0.05% NonidetP40, Roche Complete protease inhibitor, and 0.1% BSA) before analysis by Western blotting.

Western blot analysis: SDS-PAGE and Western blotting were carried out according to standard procedures. Antibodies were used at the following dilutions: anti-acetylated α-tubulin (Sigma Aldrich T6793) 1:1 000, anti-CFAP43 (27D5) 1:10, anti-CFAP43 (P4) 1:100, and anti-β-actin (MP Biomedicals 69,100) 1:1 000 000. Primary antibodies were detected using POD-labelled secondary antibodies: anti-mouse-POD (Amersham NA931), anti-rabbit-POD (Amersham NA934), and anti-rat-POD (Amersham NA935). Western blots were developed using WesternBright Quantum (Advansta).

Determination of cilia length in multiciliated cells of the trachea: Tracheas of each three 4 months old wt and *Cfap43*$^{\Delta ex3}$ mice were dissected and mTECs isolated and stained using anti-acetylated α-tubulin as described above. Cells were imaged using a confocal microscope (Leica TCS SP8 AOBS) and cilia length was determined using FIJI (Schindelin et al., 2012) by measuring the length of the ciliary tuft of each cell at three locations and averaging the measurements. For each individual, twenty cells were analyzed.

Analysis of ciliary beat frequency (CBF) and cilia-generated flow in mouse trachea: Tracheas of 6–9 months old mice were dissected as shown in Fig. S7A and described in Francis and Lo, (2013) (Francis and Lo, 2013). Two reinforcing rings (AVERY, Zweckform) were pasted into the middle of a 35 mm glass bottom Petri dish (MatTek, P35G-1.5-20-C) creating a chamber for recordings. Trachea samples were placed luminal side down into the chamber filled with Leibovitz's L-15 (Gibco) medium and covered with a 15 mm cover glass. Multiciliated cells were recorded using the Andor sCMOS Zyla camera and Nikon Spinning Disk confocal microscope (Nikon Eclipse Ti, Yokogawa/Andor) using the 100x objective. DIC optics was used to image ciliary beating for 9 s at frame rates of 156–168 fps (frames per second) at 24–27 °C. CBF was determined using FIJI as described in (Drummond, 2009). A line was set parallel to the cell membrane (Fig. S7Ba, c; Movie S4) and gray values underneath the line were represented in a single row of pixels in a kymograph (Fig. S7Bb, d) using the FIJI KymoResliceWide plugin (https://imagej.net/KymoResliceWide). The values for each pixel were plotted and imported to MATLAB (MathWorks). The Fast Fourier Transform algorithm of

MATLAB was used to extract the frequency responses of the measured signals. The double-sided magnitude of the transform was computed and normed to the length of the input signal. The single-sided spectrum of the symmetrical FFT outcome was used and multiplied by two to calculate the signals amplitudes. The highest peak amplitude in the power spectrum between 0 Hz and half the frequency of acquisition (frame rate) was used to determine the CBF. Beads (1:1000, Polysciences, Inc., Fluoresbrite Multifluorescent Microspheres 0.5 micron) were added to the trachea explants and the bead flow was recorded at 5 fps for 10 s at 24–27 °C using fluorescent microscopy. CGF in the determined region of interest (ROI) (Fig. S7C) was analyzed using the IMARIS (bitplane) 2D particle tracking tool.

Determination of ciliary flow in lateral ventricles: Brains were explanted at P7 and placed into Leibovitz's L-15 medium (Invitrogen) supplemented with FBS (Invitrogen). For analysis of ciliary flow at the floor of the lateral ventricles, the brain hemispheres exposing the lateral ventricles were transferred in medium enriched with 1 μm yellow-green FluoSpheres carboxylate (1:1000, Invitrogen). Flow was recorded for 30 s at 200 fps. Analysis of particle speed was performed using IMARIS (bitplane) using the 2D particle tracking tool.

Statistical analyses: Statistical analyses (students's t-test, One-way ANOVA) were performed using Prism (Graphpad). Data are given as mean ± SD.

Liquid chromatography fractionation and mass spectrometry: CFAP43 was immunoprecipitated from mouse testis using the Thermo Scientific Pierce crosslink IP kit with antibody P4. Immunoprecipitated CFAP43 complexes were isolated, purified, and subsequently analyzed by LC-MS/MS as described previously (Beyer et al., 2018). The full mass spectrometry proteomics data have been deposited to the ProteomeXchange Consortium via the PRIDE (Vizcaíno et al., 2016) partner repository with the dataset identifier PXD015425.

5.2. Xenopus methods

Microinjections: Xenopus laevis embryos were bilaterally injected into the neural (hydrocephalus), axial mesoderm (laterality), paraxial mesoderm (kidney) or epidermal cell lineage at the 4 cell stage. Drop size was calibrated to 4 nl per injection and *Alexa Fluor* 488 dextran (MW 70,000 or 10,000, respectively, 0.5–1 μg/μl, Thermo Fisher Scientific) was added as lineage tracer. Two different *cfap43* morpholino oligomers were used, targeting the translation start site (TBMO; 5′-CAGAGCACAGCCGGAGTTTTCCATC-3′) or the splice donor site of exon 1 (SBMO; 5′-TATTACTTTAGTCTGCCGGTTTACC-3′).

In situ hybridization in whole mounts (WISH) and on histological sections: WISH was performed using standard procedures as described elsewhere (Kawai and Hayashizaki, 2003). For histological sections, embryos were embedded in a gelatin-albumin mix and sectioned with a vibratome (Leica) at 30 μm.

Statistical analysis of Xenopus phenotypes: All measurements were performed using FIJI. Statistical calculation of organ situs defects and cyst analysis was performed using chi square (http://www.physics.csbsju.edu/stats/contingency_NROW_NCOLUMN_form.html). p-values of ventricular perimeter were calculated via Wilcoxon-Match-Pair test in RStudio.

CRISPR/Cas9 mediated genome editing: Single guide RNAs (sgRNAs) were designed using the CRISPRscan algorithm (Moreno-Mateos et al., 2015). sgRNAs targeting exon 4 and 5 were transcribed using the MEGAshortscript T7 Kit (Invitrogen) from synthetic DNA oligomers and purified with the MEGAclear Transcription Clean-Up Kit (Invitrogen). Embryos were injected with 1 ng Cas9 (PNA Bio) and 300 pg sgRNA at the 1-cell stage. Following injections, embryos were cultivated at room temperature. Direct sequencing of PCR products was applied to confirm genome editing. Groups of 10 embryos each were pooled at stage 45, DNA was isolated and gene-specific primers were used to amplify targeted sequences of *foxj1* and *cfap43*, respectively. Knockout efficiency was calculated using Synthego ICE online tool ((“https://tools.synthego.com/#/,” n.d.).

High-speed video microscopy of Xenopus laevis epidermal cilia: Control, morphant or crispant specimens were analyzed for epidermal ciliary beating patterns at stage 32. Embryos were mounted on a slide containing a rectangular chamber constructed from duct tape. Ciliary beating was recorded for 1 s at the most ventral proportion of the embryos using a high-speed Hamamatsu video camera Orca flash 4.0 at 800 fps (frames per second). For analysis of ciliary flow, 1 μm fluorescent beads (Invitrogen FluoSpheres; 1:2000) were added to the culture medium and specimens were imaged using a Zeiss Axiocam HSm camera at 175 fps. Evaluation of CBF and ciliary flow was as described in the respective mouse methods.

Immunofluoresence staining: Embryos were fixed at stage 32 in 4% PFA in PBS for 2 h at RT and washed before immunostaining. Basal feet and basal bodies were marked using anti-Tubg1 (γ-Tubulin, clone GTU-88, mouse IgG1, 1:1000) and centrin GFP DNA. Pictures were taken with a Zeiss LSM710 confocal microscope.

Determination of ventricle perimeter: Xenopus embryos were fixed in MEMFA at stage 45 or stage 48. After fixation, embryos were washed in PBS and bisected in the middle of the 4th ventricle. Ventricle perimeter were determined using FIJI.

Critical materials and resources are provided in the key resource table.

Reagent or resource	Source	Identifier
Antibodies		
acetylated α-tubulin	Sigma Aldrich	Cat.#T6793; RRID: AB_477585
AKAP3	Proteintech	Cat.#13907-1-AP; RRID:AB_2273887
β-Actin	MP Biomedicals	Cat.#69100
CoxIV	Abcam	Cat.#ab202554
Septin7	IBL international	Cat.#18991; RRID:AB_10705434
Glutamylated tubulin	AdipoGen	Cat.#AG-20B-0020-C100
Mouse-Alexa555	Invitrogen	Cat.#A21424; RRID:AB_141780
Rat-Alexa555	Invitrogen	Cat.#A11006; RRID:AB_2534074
Rabbit-Alexa488	Invitrogen	Cat.#11034; RRID:AB_2576217
Mouse-POD	Amersham	

(*continued on next page*)

(*continued*)

Reagent or resource	Source	Identifier
		Cat.#NA931; RRID:AB_772210
Rabbit-POD	Amersham	Cat.#NA934; RRID:AB_772206
Rat-POD	Amersham	Cat.#NA935; RRID:AB_772207
CFAP43 5B1 (monoclonal)	This paper	N/A
CFAP43 22A11 (monoclonal)	This paper	N/A
CFAP43 27D5 (monoclonal)	This paper	N/A
CFAP43 P4 (polyclonal)	This paper	N/A
gamma tubulin (Tubg1)	Sigma Aldrich	Prod.#T6557-100UL
Bacterial and Virus Strains		
E.coli XL1 blue for cloning		
E.coli BL21(DE3) for protein recombinant expression		
Chemicals, Peptides, and Recombinant Proteins		
MBP-CFAP43 aa1053-1226 (generation of monoclonal ABs)	This paper	N/A
CEKIARERYDNQLKQ (generation of polyclonal AB)	This paper	N/A
DAPI	AppliChem	Cat.#A4099
PNA-lectin	Invitrogen	Cat.#L32460
Pfu DNA Polymerase	Promega	M7741
Taq DNA Polymerase	Promega	M3001
FluoSpheres carboxylate 1.0 μM yellow-green (505/515)	Invitrogen	F8823
Cas9 protein from Streptococcus pyogenes with NLS	PNA Bio	CP01
Critical Commercial Assays		
Superscript IV Reverse Trancriptase	Invitrogen	Cat.#18090050
TriReagent	SigmaAldrich	Cat.#T9424
PAS staining kit	SigmaAldrich	Cat.#1016460001
DIG RNA labelling kit	Roche	Cat.#11175025910
Prime-It II Random primer labelling	Agilent	Cat.#300385
Expand High Fidelity PCR system	Roche	Cat.#11732641001
MEGAclear Transcription Clean-Up Kit	Invitrogen	AM1908
MEGAshortscrip T7 Transcription Kit	Invitrogen	AM1354
Deposited Data		
Mass spectrometry results	This Paper	ProteomeXchange Consortium: PXD015425
Experimental Models: Cell Lines		
Hamster: CHO cells	ATCC	CRL-11268
Mouse: L-cells	ATCC	CRL-2648
Mouse: L-cells (inducible CFAP43 expression)	This paper	N/A
Mouse: ES cells	Own laboratory	N/A
Experimental Models: Organisms/Strains		
Mouse: CD1	Charles River Laboratories	N/A
Mouse: 129Sv/CD1 hybrids	Own colony	N/A
Mouse: C57/BL6		
Mouse: FLPe	Rodríguez et al. (2000)	MGI:2448985
Mouse: ZP3:Cre	De Vries et al. (2000)	MGI:2176187
Mouse: *Cfap43Δex3*	This paper	N/A
Rat: LOU/C		
Xenopus laevis	Nasco	LM00715/LM00535
Oligonucleotides		
Cfap RT-PCR fwd: TCTACGGGAAGAACTGGTGG	This paper	N/A
Cfap RT-PCR rev: AGCTTGCTGCTTGGAGATGT	This paper	N/A
Foxj1 RT-PCR fwd: CTTCTGCTACTTCCGCCATGC	This paper	N/A
Foxj1 RT-PCR rev: TCCTCCTGGGTCAGCAGTAAGG	This paper	N/A
Hprt RT-PCR fwd: GCTGGTGAAAAGGACCTCT	This paper	N/A

(*continued on next page*)

(*continued*)

Reagent or resource	Source	Identifier
Hprt RT-PCRrev: CACAGGACTAGAACACCTGC	This paper	N/A
gRNA fwd: CACCGTCATCTGGATGTGACAGTCC	This paper	N/A
gRNArev: AAACGGACTGTCACATCCAGATGAC	This paper	N/A
Screen loxP sites fwd1: AATAGCAGGCATGCTGGGGATG	This paper	N/A
Screen loxP sites rev1: GGGACTTACCAGAGGGCCAGC	This paper	N/A
Screen loxP sites fwd2: GGATCCGACAGTCCTGGATTGTGTCTT	This paper	N/A
Screen loxP sites rev2: GAAAGTTAACCTTCCCATCATCCCCTG	This paper	N/A
5′ southern probe generation fwd: AAGTACGAGAAGGAGGTAGTAAGGC	This paper	N/A
5′ southern probe generation rev: TAGATCACACGAAGTGTTCTGTCC	This paper	N/A
3′ southern probe generation fwd: TAAATAAGGATTGCGATCTTTTTAGGA	This paper	N/A
3′ southern probe generation rev: GGCCATGGGGTCTGCTCAC	This paper	N/A
Genotyping mice + targeting construct fwd: GCTCTATGGCTTCTGAGGCGG	This paper	N/A
Genotyping mice + targeting construct rev: GGGACTTACCAGAGGGCCAGC	This paper	N/A
Genotyping mice *Cfap43*^{loxP} fwd: TCACCCGGCCTCCCCAAG	This paper	N/A
Genotyping mice *Cfap43*^{loxP} rev: TCCAGGACTGTCGGATCCACCT	This paper	N/A
Genotyping mice *Cfap43*$^{\Delta ex3}$ fwd: GCCAGTCACTAGGGAAAGGGAAGC	This paper	N/A
Genotyping mice *Cfap43*$^{\Delta ex3}$ rev: TCCGGTGAAACCAGGGGTCAG	This paper	N/A
Morpholino: cfap43 TBMO CAGAGCACAGCCGGAGTTTTCCATC	This paper	N/A
Morpholino: cfap43 SBMO TATTACTTTAGTCTGCCGGTTTACC	This paper	N/A
sgRNA template reverse oligo AAAAGCACCGACTCGGTGCCACTTTTTCAAGTTGATAACGGACTAGCCTTA TTTTAACTTGCTATTTCTAGCTCTAAAAC	This paper	N/A
cfap43 sgRNA1 template forward oligo CCTCACTGGGAAGTTTGACTGGC	This paper	N/A
cfap43 sgRNA1 forward primer AACAGTTCGCGACATCTCTAC	This paper	N/A
cfap43 sgRNA1 reverse primer AAATTGTTGGGGTGCATACGA	This paper	N/A
cfap43 sgRNA2 template forward oligo CCAGTGAGAGATCTCTTACTGTG	This paper	N/A
cfap43 sgRNA2 forward primer AGATCTCCGCTTCATCATCACCCA	This paper	N/A
cfap43 sgRNA2 reverse primer GCATTCTGCCAAGATTTCACCT	This paper	N/A
foxj1.S/L sgRNA template forward oligo GCAGCTAATACGACTCACTATAGGGATACATACCTGCCAGGTGTTTTAGAGCTAGAAATAGCAAG	This paper	N/A
foxj1.L forward primer CGTGGGTAAGACGCCTTCAT	This paper	N/A
foxj1.L reverse primer GGGCAAAGCAGCACGTTTAT	This paper	N/A
foxj1.S forward primer CTCCCATGGTTACAGGCAGC	This paper	N/A
foxj1.S reverse primer CCTCAGCACTACAAAAGCAGC	This paper	N/A
Recombinant DNA		
Cfap43 FANTOM plasmid (*in situ* probe generation)	Kawai and Hayashizaki (2003)	PX00616F12
pTet-On Advanced vector (inducible expression in L-cells)	Clontech	Cat.#631069
pTRE-Tight vector (inducible expression in L-cells)	Clontech	Cat.#631059
Cas9 Caspase (pX330) (ES-cell targeting)	Addgene, Cong et al., 2013	Cat.#44230
	This paper	N/A

(*continued on next page*)

(*continued*)

Reagent or resource	Source	Identifier
Cfap43 targeting vector derived from pBluescript		
pMAL-C (Recombinant protein expression in *E. coli*)	NEB	Cat.#N8108S
Software and Algorithms		
FIJI (ImageJ)	Schindelin et al. (2012)	RRID:SCR_002285
Prism	GraphPad	RRID:SCR_002798
Imaris	Bitplane	RRID:SCR_007370
MATLAB	MathWorks	RRID:SCR_001622
MacVector	MacVector	RRID:SCR_015700
Photoshop	Adobe	RRID:SCR_014199
Illustrator	Adobe	RRID:SCR_010279
Chi-square		http://www.physics.csbsju.edu/stats/contingency_NROW_NCOLUMN_form.html
Synthego ICE	Synthego	https://ice.synthego.com/
Other		

Authors' contributions

ER, AB, and LT performed experiments in mice and cell culture, KSG generated and analyzed mutant mice, TO and FF performed experiments in *Xenopus*, and - together with AB and LT - the analysis of ciliary motility of mutant mouse ventricles at P7. JH performed the TEM analyses. KB and MU performed the mass spectrometric analysis, MM characterized polyclonal antibodies and generated cell line with inducible CFAP43 expression, EK generated monoclonal antibodies. AG and MB planned and supervised experiments, analyzed data together with ER, AB, TO, FF and LT, and wrote the manuscript with suggestions from all authors.

Acknowledgements

We thank S. Brody (Washington University, St. Louis) for *Foxj1* mice; Feng Zhang for plasmid pX330; R. Bauerfeind for the introduction into the Nikon Spinning Disk and the help with cilia recordings; J. Gieseke for help with MATLAB (MathWorks). This work was financially supported by DFG grant GO 449/14-1 and BL 285/14-1 to AG and MB as well as by the DFG Cluster of Excellence "REBIRTH" to AG. TO was the recipient of a Ph.D. fellowship from the Landesgraduiertenförderung Baden-Württemberg. MU was supported by the Tistou & Charlotte Kerstan Stiftung.

Appendix A. Supplementary data

Supplementary data to this article can be found online at https://doi.org/10.1016/j.ydbio.2019.12.010.

References

Abdelhamed, Z., Vuong, S.M., Hill, L., Shula, C., Timms, A., Beier, D., Campbell, K., Mangano, F.T., Stottmann, R.W., Goto, J., 2018. A mutation in Ccdc39 causes neonatal hydrocephalus with abnormal motile cilia development in mice. Development 145, dev154500. https://doi.org/10.1242/dev.154500.

Afzelius, B., 1959. Electron microscopy of the sperm tail; results obtained with a new fixative. J. Biophys. Biochem. Cytol. 5, 269–278.

Alten, L., Schuster-Gossler, K., Beckers, A., Groos, S., Ulmer, B., Hegermann, J., Ochs, M., Gossler, A., 2012. Differential regulation of node formation, nodal ciliogenesis and cilia positioning by Noto and Foxj1. Development 139, 1276–1284. https://doi.org/10.1242/dev.072728.

Banizs, B., Pike, M.M., Millican, C.L., Ferguson, W.B., Komlosi, P., Sheetz, J., Bell, P.D., Schwiebert, E.M., Yoder, B.K., 2005. Dysfunctional cilia lead to altered ependyma and choroid plexus function, and result in the formation of hydrocephalus. Development 132, 5329–5339. https://doi.org/10.1242/dev.02153.

Beyer, T., Bolz, S., Junger, K., Horn, N., Moniruzzaman, M., Wissinger, Y., Ueffing, M., Boldt, K., 2018. CRISPR/Cas9-mediated genomic editing of cluap1/IFT38 reveals a new role in actin arrangement. Mol. Cell. Proteom. 17, 1285–1294. https://doi.org/10.1074/mcp.RA117.000487.

Blum, M., Ott, T., 2018a. Animal left–right asymmetry. Curr. Biol. 28, R301–R304. https://doi.org/10.1016/j.cub.2018.02.073.

Blum, M., Ott, T., 2018b. Xenopus: an undervalued model organism to study and model human genetic disease. Cells Tissues Organs 205, 303–313. https://doi.org/10.1159/000490898.

Brody, S.L., Yan, X.H., Wuerffel, M.K., Song, S.K., Shapiro, S.D., 2000. Ciliogenesis and left-right axis defects in forkhead factor HFH-4-null mice. Am. J. Respir. Cell Mol. Biol. 23, 45–51. https://doi.org/10.1165/ajrcmb.23.1.4070.

Cong, L., Ran, F.A., Cox, D., Lin, S., Barretto, R., Habib, N., Hsu, P.D., Wu, X., Jiang, W., Marraffini, L.A., Zhang, F., 2013. Multiplex genome engineering using CRISPR/Cas systems. Science 339, 819–823. https://doi.org/10.1126/science.1231143.

Consortium, UniProt, 2019. UniProt: a worldwide hub of protein knowledge. Nucleic Acids Res. 47, D506–D515. https://doi.org/10.1093/nar/gky1049.

Coutton, C., Vargas, A.S., Amiri-Yekta, A., Kherraf, Z.-E., Ben Mustapha, S.F., Le Tanno, P., Wambergue-Legrand, C., Karaouzène, T., Martinez, G., Crouzy, S., Daneshipour, A., Hosseini, S.H., Mitchell, V., Halouani, L., Marrakchi, O., Makni, M., Latrous, H., Kharouf, M., Deleuze, J.-F., Boland, A., Hennebicq, S., Satre, V., Jouk, P.-S., Thierry-Mieg, N., Conne, B., Dacheux, D., Landrein, N., Schmitt, A., Stouvenel, L., Lorès, P., Khouri, El, E., Bottari, S.P., Fauré, J., Wolf, J.-P., Pernet-Gallay, K., Escoffier, J., Gourabi, H., Robinson, D.R., Nef, S., Dulioust, E., Zouari, R., Bonhivers, M., Touré, A., Arnoult, C., Ray, P.F., 2018. Mutations in CFAP43 and CFAP44 cause male infertility and flagellum defects in Trypanosoma and human. Nat. Commun. 9, 686. https://doi.org/10.1038/s41467-017-02792-7.

Cruz, C., Ribes, V., Kutejova, E., Cayuso, J., Lawson, V., Norris, D., Stevens, J., Davey, M., Blight, K., Bangs, F., Mynett, A., Hirst, E., Chung, R., Balaskas, N., Brody, S.L., Marti, E., Briscoe, J., 2010. Foxj1 regulates floor plate cilia architecture and modifies the response of cells to sonic hedgehog signalling. Development 137, 4271–4282. https://doi.org/10.1242/dev.051714.

de Vries, W.N., Binns, L.T., Fancher, K.S., Dean, J., Moore, R., Kemler, R., Knowles, B.B., 2000. Expression of Cre recombinase in mouse oocytes: a means to study maternal effect genes. Genesis 26, 110–112.

del Viso, F., Khokha, M., 2012. Generating diploid embryos from Xenopus tropicalis. Methods Mol. Biol. 917, 33–41. https://doi.org/10.1007/978-1-61779-992-1_3.

Drummond, I., 2009. Studying cilia in zebrafish. Methods Cell Biol. 93, 197–217. https://doi.org/10.1016/S0091-679X(08)93011-9.

Dubaissi, E., Papalopulu, N., 2011. Embryonic frog epidermis: a model for the study of cell-cell interactions in the development of mucociliary disease. Disease Models & Mechanisms 4, 179–192. https://doi.org/10.1242/dmm.006494.

Dubaissi, E., Rousseau, K., Lea, R., Soto, X., Nardeosingh, S., Schweickert, A., Amaya, E., Thornton, D.J., Papalopulu, N., 2014. A secretory cell type develops alongside multiciliated cells, ionocytes and goblet cells, and provides a protective, anti-infective function in the frog embryonic mucociliary epidermis. Development 141, 1514–1525. https://doi.org/10.1242/dev.102426.

El-Brolosy, M.A., Kontarakis, Z., Rossi, A., Kuenne, C., nther, S.G.X., Fukuda, N., Kikhi, K., Boezio, G.L.M., Takacs, C.M., Lai, S.-L., Fukuda, R., Gerri, C., Giraldez, A.J., Stainier, D.Y.R., 2019. Genetic compensation triggered by mutant mRNA degradation. Nature 1–26. https://doi.org/10.1038/s41586-019-1064-z.

Francis, R., Lo, C., 2013. Ex vivo method for high resolution imaging of cilia motility in rodent airway epithelia. J Vis Exp e50343. https://doi.org/10.3791/50343.

Fu, G., Wang, Q., Phan, N., Urbanska, P., Joachimiak, E., Lin, J., Wloga, D., Nicastro, D., 2018. The I1 dynein-associated tether and tether head complex is a conserved regulator of ciliary motility. Mol. Biol. Cell mbc.E18–02–0142. https://doi.org/10.1091/mbc.E18-02-0142.

Gerdes, J.M., Davis, E.E., Katsanis, N., 2009. The vertebrate primary cilium in development, homeostasis, and disease. Cell 137, 32–45. https://doi.org/10.1016/j.cell.2009.03.023.

Getwan, M., Lienkamp, S.S., 2017. Toolbox in a tadpole: Xenopus for kidney research [WWW Document], n.d Cell Tissue Res. 369, 143–157. https://doi.org/10.1007/s00441-017-2611-2. WWW Document. https://tools.synthego.com/#/. https://tools.synthego.com/#/. https://tools.synthego.com/#/.

Ibañez-Tallon, I., Pagenstecher, A., Fliegauf, M., Olbrich, H., Kispert, A., Ketelsen, U.-P., North, A., Heintz, N., Omran, H., 2004. Dysfunction of axonemal dynein heavy chain Mdnah5 inhibits ependymal flow and reveals a novel mechanism for hydrocephalus formation. Hum. Mol. Genet. 13, 2133–2141. https://doi.org/10.1093/hmg/ddh219.

Ikegami, K., Sato, S., Nakamura, K., Ostrowski, L.E., Setou, M., 2010. Tubulin polyglutamylation is essential for airway ciliary function through the regulation of beating asymmetry. Proc. Natl. Acad. Sci. U.S.A. 107, 10490–10495. https://doi.org/10.1073/pnas.1002128107.

Irons, M.J., Clermont, Y., 1982a. Formation of the outer dense fibers during spermiogenesis in the rat. Anat. Rec. 202, 463–471. https://doi.org/10.1002/ar.1092020405.

Irons, M.J., Clermont, Y., 1982b. Kinetics of fibrous sheath formation in the rat spermatid. Am. J. Anat. 165, 121–130. https://doi.org/10.1002/aja.1001650204.

Jacquet, B.V., Salinas-Mondragon, R., Liang, H., Therit, B., Buie, J.D., Dykstra, M., Campbell, K., Ostrowski, L.E., Brody, S.L., Ghashghaei, H.T., 2009. FoxJ1-dependent gene expression is required for differentiation of radial glia into ependymal cells and a subset of astrocytes in the postnatal brain. Development 136, 4021–4031. https://doi.org/10.1242/dev.041129.

Jain, R., Pan, J., Driscoll, J.A., Wisner, J.W., Huang, T., Gunsten, S.P., You, Y., Brody, S.L., 2010. Temporal relationship between primary and motile ciliogenesis in airway epithelial cells. Am. J. Respir. Cell Mol. Biol. 43, 731–739. https://doi.org/10.1165/rcmb.2009-0328OC.

Kawai, J., Hayashizaki, Y., 2003. DNA book. Genome Res. 13, 1488–1495. https://doi.org/10.1101/gr.914203.

Kubo, T., Hou, Y., Cochran, D.A., Witman, G.B., Oda, T., 2018. A microtubule-dynein tethering complex regulates the axonemal inner dyneinf(I1). Mol. Biol. Cell mbc.E17–11–0689. https://doi.org/10.1091/mbc.E17-11-0689.

Lee, L., 2013. Riding the wave of ependymal cilia: genetic susceptibility to hydrocephalus in primary ciliary dyskinesia. J. Neurosci. Res. 91, 1117–1132. https://doi.org/10.1002/jnr.23238.

Lin, J., Heuser, T., Song, K., Fu, X., Nicastro, D., 2012. One of the nine doublet microtubules of eukaryotic flagella exhibits unique and partially conserved structures. PLoS One 7, e46494. https://doi.org/10.1371/journal.pone.0046494.

Lindemann, C.B., Orlando, A., Kanous, K.S., 1992. The flagellar beat of rat sperm is organized by the interaction of two functionally distinct populations of dynein bridges with a stable central axonemal partition. J. Cell Sci. 102 (Pt 2), 249–260.

Lyons, R.A., Saridogan, E., Djahanbakhch, O., 2006. The reproductive significance of human Fallopian tube cilia. Hum. Reprod. Update 12, 363–372. https://doi.org/10.1093/humupd/dml012.

Moorman, A.F., Houweling, A.C., de Boer, P.A., Christoffels, V.M., 2001. Sensitive nonradioactive detection of mRNA in tissue sections: novel application of the whole-mount in situ hybridization protocol. J. Histochem. Cytochem. 49, 1–8.

Moreno-Mateos, M.A., Vejnar, C.E., Beaudoin, J.-D., Fernandez, J.P., Mis, E.K., Khokha, M.K., Giraldez, A.J., 2015. CRISPRscan: designing highly efficient sgRNAs for CRISPR-Cas9 targeting in vivo. Nat. Methods 12, 982–988. https://doi.org/10.1038/nmeth.3543.

Morimoto, Y., Yoshida, S., Kinoshita, A., Satoh, C., Mishima, H., Yamaguchi, N., Matsuda, K., Sakaguchi, M., Tanaka, T., Komohara, Y., Imamura, A., Ozawa, H., Nakashima, M., Kurotaki, N., Kishino, T., Yoshiura, K.-I., Ono, S., 2019. Nonsense mutation in CFAP43 causes normal-pressure hydrocephalus with ciliary abnormalities. Neurology. https://doi.org/10.1212/WNL.0000000000007505.

O'Callaghan, C.A., Tormo, J., Willcox, B.E., Blundell, C.D., Jakobsen, B.K., Stuart, D.I., McMichael, A.J., Bell, J.I., Jones, E.Y., 1998. Production, crystallization, and preliminary X-ray analysis of the human MHC class Ib molecule HLA-E. Protein Sci. 7, 1264–1266. https://doi.org/10.1002/pro.5560070525.

Praveen, K., Davis, E.E., Katsanis, N., 2015. Unique among ciliopathies: primary ciliary dyskinesia, a motile cilia disorder. F1000Prime Rep 7, 36. https://doi.org/10.12703/P7-36.

Quigley, I.K., Kintner, C., 2017. Rfx2 stabilizes Foxj1 binding at chromatin loops to enable multiciliated cell gene expression. PLoS Genet. 13, e1006538 https://doi.org/10.1371/journal.pgen.1006538.

Rodríguez, C.I., Buchholz, F., Galloway, J., Sequerra, R., Kasper, J., Ayala, R., Stewart, A.F., Dymecki, S.M., 2000. High-efficiency deleter mice show that FLPe is an alternative to Cre-loxP. Nat. Genet. 25, 139–140. https://doi.org/10.1038/75973.

Rudat, C., Grieskamp, T., Röhr, C., Airik, R., Wrede, C., Hegermann, J., Herrmann, B.G., Schuster-Gossler, K., Kispert, A., 2014. Upk3b is dispensable for development and integrity of urothelium and mesothelium. PLoS One 9, e112112. https://doi.org/10.1371/journal.pone.0112112.

Schindelin, J., Arganda-Carreras, I., Frise, E., Kaynig, V., Longair, M., Pietzsch, T., Preibisch, S., Rueden, C., Saalfeld, S., Schmid, B., Tinevez, J.-Y., White, D.J., Hartenstein, V., Eliceiri, K., Tomancak, P., Cardona, A., 2012. Fiji: an open-source platform for biological-image analysis. Nat. Methods 9, 676–682. https://doi.org/10.1038/nmeth.2019.

Sha, Y.-W., Wang, X., Xu, X., Su, Z.-Y., Cui, Y., Mei, L.-B., Huang, X.-J., Chen, J., He, X.-M., Ji, Z.-Y., Bao, H., Yang, X., Li, P., Li, L., 2017. Novel mutations in CFAP44 and CFAP43 cause multiple morphological abnormalities of the sperm flagella (MMAF). Reprod Sci 1933719117749756. https://doi.org/10.1177/1933719117749756.

Spassky, N., Merkle, F.T., Flames, N., Tramontin, A.D., García-Verdugo, J.M., Alvarez-Buylla, A., 2005. Adult ependymal cells are postmitotic and are derived from radial glial cells during embryogenesis. Neuroscience 25, 10–18. https://doi.org/10.1523/JNEUROSCI.1108-04.2005.

Stannard, W., O'Callaghan, C., 2006. Ciliary function and the role of cilia in clearance. J. Aerosol Med. 19, 110–115. https://doi.org/10.1089/jam.2006.19.110.

Stauber, M., Weidemann, M., Dittrich Breiholz, O., Lobschat, K., Alten, L., Mai, M., Beckers, A., Kracht, M., Gossler, A., 2017. Identification of FOXJ1 effectors during ciliogenesis in the foetal respiratory epithelium and embryonic left-right organiser of the mouse. Dev. Biol. 423, 170–188. https://doi.org/10.1016/j.ydbio.2016.11.019.

Takeda, S., Narita, K., 2012. Structure and function of vertebrate cilia, towards a new taxonomy. Differentiation 83, S4–S11. https://doi.org/10.1016/j.diff.2011.11.002.

Tang, S., Wang, X., Li, W., Yang, X., Li, Z., Liu, W., Li, C., Zhu, Z., Wang, L., Wang, J., Zhang, L., Sun, X., Zhi, E., Wang, H., Li, H., Jin, L., Luo, Y., Wang, J., Yang, S., Zhang, F., 2017. Biallelic mutations in CFAP43 and CFAP44 cause male infertility with multiple morphological abnormalities of the sperm flagella. Am. J. Hum. Genet. 100, 854–864. https://doi.org/10.1016/j.ajhg.2017.04.012.

Urbanska, P., Joachimiak, E., Bazan, R., Fu, G., Poprzeczko, M., Fabczak, H., Nicastro, D., Wloga, D., 2018. Ciliary proteins Fap43 and Fap44 interact with each other and are essential for proper cilia and flagella beating. Cell. Mol. Life Sci. 100, 2008. https://doi.org/10.1007/s00018-018-2819-7.

Vizcaíno, J.A., Csordas, A., del-Toro, N., Dianes, J.A., Griss, J., Lavidas, I., Mayer, G., Perez-Riverol, Y., Reisinger, F., Ternent, T., Xu, Q.-W., Wang, R., Hermjakob, H., 2016. 2016 update of the PRIDE database and its related tools. Nucleic Acids Res. 44, D447–D456. https://doi.org/10.1093/nar/gkv1145.

Walentek, P., Quigley, I.K., 2017. What we can learn from a tadpole about ciliopathies and airway diseases: using systems biology in Xenopus to study cilia and mucociliary epithelia. Genesis 55, e23001. https://doi.org/10.1002/dvg.23001.

Wolf, E., Kim, P.S., Berger, B., 1997. MultiCoil: a program for predicting two- and three-stranded coiled coils. Protein Sci. 6, 1179–1189. https://doi.org/10.1002/pro.5560060606.

Yoshiba, S., Hamada, H., 2014. Roles of cilia, fluid flow, and Ca2+ signaling in breaking of left-right symmetry. Trends Genet. 30, 10–17. https://doi.org/10.1016/j.tig.2013.09.001.

You, Y., Brody, S.L., 2013. Culture and differentiation of mouse tracheal epithelial cells. Methods Mol. Biol. 945, 123–143. https://doi.org/10.1007/978-1-62703-125-7_9.

Zein, El, L., Ait-Lounis, A., Morle, L., Thomas, J., Chhin, B., Spassky, N., Reith, W., Durand, B., 2009. RFX3 governs growth and beating efficiency of motile cilia in mouse and controls the expression of genes involved in human ciliopathies. J. Cell Sci. 122, 3180–3189. https://doi.org/10.1242/jcs.048348.